Mathematical modeling in elastography.

Anastasia Kozhemyak

Thèse pour l'obtention du titre de

DOCTEUR DE L'ÉCOLE POLYTECHNIQUE

Spécialité : Mathématiques Appliquées

présentée et soutenue par

Anastasia KOZHEMYAK

Mathematical Models and Reconstruction Methods for Emerging Biomedical Imaging Techniques

Jury

Ioan	IONESCU	(Président du jury)
Mark	ASCH	(Rapporteur)
Vilmos	KOMORNIK	(Rapporteur)
Habib	AMMARI	(Directeur de thèse)
Kamel	HAMDACHE	(Examinateur)
Roman	NOVIKOV	(Examinateur)

ÉCOLE POLYTECHNIQUE – CENTRE DE MATHÉMATHIQUES APPLIQUÉES

13 juin 2008

Remerciements

Je tiens en premier lieu à remercier très chaleureusement Habib Ammari, mon directeur de thèse, pour son soutien au cours de ces quatre années. Son ouverture scientifique, sa rigueur, son enthousiasme toujours très communicatif, ses critiques et ses encouragements sont pour beaucoup dans ce travail.

Je remercie tous les membres du jury du temps qu'ils m'ont consacré. Mes remerciements vont tout particulièrement à Marc Asch et à Vilmos Komornik qui ont accepté la tâche de rapporteur. Ma reconnaissance va également à Ioan Ionescu pour avoir accepté la présidence de mon jury.

Je voudrais exprimer ma reconnaissance à Sylvain Ferrand pour son aide en informatique.

Toute ma gratitude va à toutes les autres personnes qui m'ont aidée et qui ont contribué à l'enrichissement de ce travail.

Je termine ici en dédiant ce mémoire à toute ma famille pour leurs encouragements précieux et en particulier à Alexey et à Ivan pour leur patience.

Contents

Introduction

Présentation générale

L'apparition de techniques avancées en imagerie a amélioré de manière significative la qualité de la surveillance médicale des patients. Les modalités d'imagerie non-invasives permettent aux médecins de faire des diagnostics plus précis et plus précoces et de prescrire des modes de traitement plus performants et plus justes. De multiples modalités d'imagerie sont employées actuellement ou sont en cours d'étude.

Dans cette thèse, nous étudions trois techniques émergentes d'imagerie biomédicale :

- *imagerie magnéto-acoustique*;
- *imagerie thermographique*;
- *endotomographie par impédance électrique.*

Pour chacune de ces trois techniques, nous proposons des modèles mathématiques et nous présentons des nouvelles méthodes de reconstruction en imagerie médicale.

Tout d'abord, nous allons décrire les principes physiques de toutes les techniques proposées dans cette thèse.

En **imagerie magnéto-acoustique**, le signal de sonde, par exemple une onde acoustique, un courant électrique ou une tension électrique, est appliqué aux tissus biologiques qui sont placés dans un champs magnétique. Le signal induit par la force de Lorentz est une fonction de la conductivité locale des tissus biologiques. Si, par exemple, le signal de sonde est une onde acoustique alors le signal induit est un courant électrique et la force de Lorentz produit l'apparition d'une densité de courant électrique locale.

La mesure des courants électriques (a) ou de la pression (b) induits sur l'ensemble de la frontière, proportionnels à la conductivité locale, permet d'obtenir la distribution de la conductivité avec une bonne résolution. La méthode (a) est appelée l'*imagerie potentielle par vibration* ou VPT (de l'anglais *vibration potential imaging*) aussi connue

comme l'*imagerie à effet Hall*. La méthode (b) est appelée la *tomographie magnéto-acoustique à induction magnétique* ou MAT-MI (de l'anglais *magneto-acoustic tomography with magnetic induction*).

La méthode (a) peut être appliquée aux tissus du corps *in vivo*, ainsi qu'aux cellules cultivées en suspension. Le faisceau ultrasonore effectue l'excitation dans une région d'étude et le courant induit est mesuré à l'aide des électrodes. La recherche dans cette direction semble très prometteuse pour avancer la tomographie par impédence électrique ou EIT (de l'anglais *electrical impedance tomography*). La technique EIT est une technique d'imagerie qui se concentre sur la reconstruction de la distribution de l'impédance dans les tissus biologiques par l'injection de courants électriques et par la mesure non-invasive de potentiels. Dans le cadre de la technique EIT, le courant électrique est injecté dans l'objet par les électrodes surfaciques et les potentiels correspondant à la frontière sont mesurés sur toute la surface de l'objet dans le but de reconsrtuire la distribution de l'impédance à l'intérieur de l'objet. Il est bien connu que cette méthode d'imagerie de la distribution de conductivité produit des résultats avec une mauvaise précision. L'imagerie potentielle par vibration s'appuie sur des techniques de mesure innovantes qui intègrent l'information structurelle. Dans le cadre de cette méthode, la résolution intrinsèque est de l'ordre de la taille de la tâche focale de l'onde ultrasonore, alors elle devrait fournir des résultats de haute résolution.

Notons qu'une onde acoustique ou un déplacement de tissu apparaissent lorsque l'on place un tissu électriquement actif dans un champs magnétique.

Cette méthode (c), appelée l'*imagerie magnéto-acoustique de courant électrique* ou MACI (de l'anglais *magneto-acoustic current imaging*), a été proposée pour reconstruire les conductivités en detectant les courants actifs résultants de l'action de nerfs ou de fibres musculaires qui peuvent être imagés en mesurant le signal de pression induit.

L'**imagerie médicale thermique** est en train de devenir une modalité de dépistage du cancer du sein, de la peau et du foie. En tant que modalité d'imagerie physiologique qui effectue les analyses sur les fonctions du corps, elle peut permettre un diagnostic plus précoce que des examens anatomiques. La procédure de l'imagerie médicale thermique est fondée sur le principe selon lequel l'activité des vaisseaux sanguins et lymphatiques dans le tissu précancéreux et dans la zones environnantes du cancer développé est presque toujours plus élevée que dans les tissus normaux. Comme les masses précancéreuses et cancéreuses sont des tissus très métaboliques, ils ont besoin de ravitaillement abondant pour maintenir leur croissance. Pour croître les tumeurs doivent développer un nouveau circuit d'approvisionnement sanguin. En effet, les tumeurs induisent un tel système de nouveaux vaisseaux sanguins à partir de vaisseaux préexistants, processus qui se rapporte à l'angiogenèse. Ce processus se traduit par une augmentation de la température. L'expérience actuelle consiste à utiliser des caméras thermiques ultra-sensibles et des ordinateurs sophistiqués pour détecter, analyser et produire des images thermiques de diagnostic haute résolution des changements de température et vasculaires.

Le principe de l'imagerie thermique est le suivant. Un détecteur infrarouge à balayage est utilisé pour convertir le rayonnement infrarouge émis par la surface de la peau en impulsions électriques qui sont visualisées en couleurs sur un moniteur. Cette image visuelle, appelée *thermogramme*, représente graphiquement la température du corps. Comme dans le corps normal la répartition de la température est assez symétrique, la répartition anormale de température peut être facilement identifiée.

Les études cliniques montrent que l'imagerie thermique des seins a une sensitivité et précision de 90% en moyenne. Une image infrarouge anormale est le plus important marqueur de risque élevé de développement du cancer du sein. L'imagerie thermique peut être utilisée

(i) pour définir l'étendue de la lésion dont le diagnostic a été déjà fait;

(ii) pour la localisation d'un domaine anormal non préalablement identifié, dans le but d'effectuer les tests de diagnostique suivants;

(iii) pour détecter précocement les lésions avant qu'elles ne soient cliniquement évidentes;

(iv) pour guider les thérapies parmi lesquelles les plus connues sont les nouvelles techniques de thermo-ablation des tumeurs.

L'imagerie thermique ultrasonore est une technique prometteuse qui utilise la thermographie. Elle exploite le principe de dépendance de la vitesse du son dans un milieu vis-à-vis de la température. Les techniques de thermo-ablation, telle que la chirurgie par ultrasons focalisés, vise à détruire les tumeurs malignes sans endommager les tissus environnants.

La technique consiste, dans un premier temps, à utiliser le système de la chirurgie par ultrasons focalisés à basse intensité et utiliser en même temps le système de diagnostique d'imagerie thermique ultrasonore pour détecter l'augmentation locale de la température en supposant que la dépendance de la vitesse du son vis-à-vis de la température est connue.

L'**endotomographie par impédance électrique** ou EIET (de l'anglais *electrical impedance endo-tomography*) est une méthode pour reconstruire la conductivité des tissus ou des organes profonds en utilisant une sonde d'impédance située au centre de la région d'étude. La sonde est constituée d'électrodes parallèles, placées à la surface d'un cylindre isolant et le champ électrique se propage dans le milieu entourant la sonde. Cette nouvelle méthode a été développee pour la détection du cancer de la prostate. Le principe de l'endotomographie suppose que le tissu normal de la prostate et le tissu de la tumeur ont des conductivités électriques très différentes.

Dans la pratique, le nombre des couples de courants et des potentiels électriques capturés doivent être limités en fonction du nombre d'électrodes fixées sur la surface de la sonde ce qui restreint la résolution de l'image. Nous pouvons certainement augmenter la résolution de l'image de conductivité en augmentant le nombre d'électrodes. Néanmoins, il faut remarquer qu'au-delà d'un certain niveau, l'augmentation du nombre d'électrodes ne peut pas améliorer la résolution de l'image à l'intérieur du corps à cause de l'inévitable bruit de mesure et de l'insensibilité intrinsèque mentionnée auparavant. Dans sa forme la plus

générale EIET est sévèrement mal posée et non linéaire. Ces difficultés majeures et fondamentales peuvent être mises en évidence par les propriétés de la valeur moyenne dans le cadre de la théorie des équations aux dérivées partielles elliptiques. En effet, la valeur du potentiel à chaque point dans le milieu environnant la sonde peut être exprimée comme une moyenne pondérée de potentiels voisins où le poids est déterminé par la distribution de conductivité. Dans ce mode de calul de moyenne pondérée, les valeurs de potentiels mesurées par la sonde sont influencées par la distribution de conductivité. Par conséquent, les mesures de la sonde sont reliées à la distribution de conductivité de façon fortement non linéaire. C'est le principal obstacle au développement des algorithmes de reconstruction non-itératifs en présence de limitation de données. Cependant, si nous avons d'autres informations structurelles sur le milieu, alors nous pourrons peut-être déterminer les caractéristiques spécifiques sur la distribution de conductivité avec une bonne résolution. Par exemple, on peut supposer qu'il existe un certain nombre de petites inclusions de conductivités nettement différentes de celle du fond. Cette situation se présente par exemple dans le cadre de l'imagerie du cancer de la prostate.

Dans ce cas, EIET cherche à restituer les inclusions inconnues. Grâce à la petite taille des inclusions les potentiels associés mesurés à la surface de la sonde sont très proches de potentiels correspondant au milieu sans inclusions. A moins que l'on sâche exactement quel échantillon doit être restitué, il est presque impossible d'extraire de données largement bruitées des informations pertinentes sur les inclusions. En outre, en imagerie de la prostate, il n'est en général pas nécessaire de reconstituer la conductivité ou de reconstruire la géométrie des inclusions avec une très grande précision. L'intérêt majeur consiste à déterminer leurs positions et leurs tailles.

Plan de la thèse

Dans le chapitre 1, après avoir rappelé les bases théoriques des trois approches différentes de l'imagerie magnéto-acoustique, nous proposons de nouveaux algorithmes pour résoudre des problèmes inverses correspondant à chaque approche.

Le chapitre 2 est consacré à l'imagerie thermographique. Nous effectuons une étude quantitative de la perturbation de température due à une petite inclusion et nous concevons de nouveaux algorithmes pour la localisation et l'estimation de la taille de l'inclusion. Nous adoptons un modèle assez réaliste; toute la théorie basée sur ce modèle peut donc être appliquée aux autres domaines de thermographie, en particulier à la résolution des problèmes de détection des inclusions. Notre but est de fournir un terrain mathématique pour la reconstruction grossière d'une caractéristique de l'inclusion qui soit stable à travers tous les bruits appliqués aux mesures et à travers toutes les modifications de la géométrie. Etant basé sur des estimations rigoureuses, nous suggérons une approximation qui permet de développer un algorithme non itératif de détection d'inclusions. Nous proposons une nouvelle plate-forme mathématique de l'imagerie thermique ultrasonore qui peut être utilisée pour guider les nouvelles thérapies, par exemple la thermo-ablation des tumeurs.

Dans le chapitre 3, nous étudions l'endotomographie par impédance électrique. Nous avon trois objectifs:

(i) Nous proposons une procédure de détection d'une inclusion isotrope de forme elliptique dont le premier ordre du tenseur de polarisation anisotrope ou APT (de l'anglais *anisotropic polarisation tensor*) coïncide avec celui d'une inclusion anisotrope en forme de disque. Ensuite, nous montrons comment il est possible d'extraire la caracteristique de l'anisotropie à partir d'APT d'ordre suppérieur.

(ii) Nous proposons également l'extension de l'approche de l'imagerie par déformation élastique au cas de EIET et nous démontrons sa faisabilité. Cette approche appelée *impédiographie* est basée sur la mesure simultanée d'un potentiel et des vibrations acoustiques induits par une onde ultrasonore. Sa résolution intrinsèque dépend de la taille de la tâche focale de la perturbation acoustique, elle fournit donc des images de haute résolution. L'idée principale de l'impédiographie consiste à extraire le maximum d'informations sur la distribution de conductivité à partir de données qui ont été enrichies par le couplage des mesures électriques et de la localisation des perturbations élastiques. Plus précisement, on perturbe le milieu au cours de l'acquisition des mesures électriques, en effectuant la focalisation ultrasonore sur la région d'intérêt de petite taille à l'intérieur du corps. En utilisant un modèle simple pour les effets mécaniques de l'onde ultrasonore, on peut démontrer que la différence entre les mesures dans les cas perturbé et non perturbé est asymptotiquement égale à la valeur de la densité d'énergie au centre de la zone perturbée. Dans la pratique, des ondes ultrasonores influencent une zone de quelque millimètres de diamètre. Les perturbations devraient donc être sensibles aux variations de la conductivité à l'échelle millimétrique, précision requise pour la diagnostique du cancer de la prostate.

(iii) Nous présentons la méthode de détection de multiple inclusions en utilisant le modèle réaliste.

General presentation

The introduction of advanced imaging techniques has significantly improved the quality of medical care available to patients. Noninvasive imaging modalities allow a physician to make increasingly accurate diagnoses and render precise and measured modes of treatment. A multitude of imaging modalities are available currently on subject of active and promising research.

In this thesis, we investigate the following three emerging biomedical imaging techniques:

(i) Magneto-Acoustic Imaging;

(ii) Thermographic Imaging;

(iii) Electrical Impedance Endo-Tomography.

For each of these techniques, we propose mathematical models and build new methodology for image reconstruction.

First of all we outline the physical principle of these techniques.

In **magneto-acoustic imaging**, a probe signal such as an acoustic wave or an electric current (or voltage) is applied to a biological tissue placed in a magnetic field. The probe signal produces by the Lorentz force an induced signal that is a function of the local electrical conductivity of the biological tissue. If the probe signal is an acoustic wave, then the induced signal is an electric current and the Lorentz force causes a local current density.

Induced boundary currents (a) or pressure (b) which are proportional to the local electrical conductivity can be measured to reconstruct the conductivity distribution with the spatial resolution of the ultrasound. The induced signal is detected and an image of the local electrical conductivity of the specimen based on the detected induced signal is generated. Method (a) is referred as the vibration potential imaging and method (b) as magneto-acoustic tomography with magnetic induction. The vibration potential imaging is also known as the Hall effect imaging.

Method (a) can be applied to body tissue *in vivo* and to measurements in suspensions and cultured cells. The ultrasound beam ensures the excitation of the desired region of interest and the interaction current is collected by means of electrodes. It is a very promising direction of research for improving the electrical impedance tomography (EIT). EIT is an imaging technique focused upon reconstructing the impedance distribution of biological tissue using current injection and noninvasive voltage measurements. In EIT, electrical current is injected into the object from electrodes attached to the surface, and the corresponding boundary voltage is measured over the surface of the object in order to reconstruct the impedance distribution within the volume. It is known that this approach for imaging the conductivity distribution produces images with deceivingly poor accuracy and spatial resolution. The vibration potential imaging relies on innovative measurement

techniques which incorporate structural information. Its intrinsic resolution is of order of the size of the focal spot of the ultrasound, and thus it should provide high resolution images.

If an electrically active tissue is placed into the magnetic field then an acoustic wave or tissue displacement is created. This method (c), known as magneto-acoustic current imaging, has been suggested as a method for reconstructing current dipoles and imaging action currents arising from active nerve or muscle fibers by detecting the induced pressure signal.

Medical thermal imaging is becoming a common screening modality in the areas of breast, skin, and liver cancers. As a physiological imaging modality that assesses body function, it can indicate developing disease states earlier than anatomical examinations. The imaging procedure is based on the principle that chemical and blood vessel activity in both pre-cancerous tissue and the area surrounding a developing cancer is almost always higher than in the normal tissue. Since pre-cancerous and cancerous masses are highly metabolic tissues, they need an abundant supply of nutrients to maintain their growth. To obtain these nutrients they increase circulation to their cells by secreting chemicals to keep existing blood vessels open, recruit dormant vessels, and create new ones (neoangiogenesis). This process results in a local increase in temperature. State-of-the-art applications use ultra-sensitive thermal imaging cameras and sophisticated computers to detect, analyze, and produce high-resolution diagnostic thermal images of these temperature and vascular changes.

The principle of thermal imaging is as follows. An infrared scanning device is used to convert infrared radiation emitted from the skin surface into electrical impulses that are visualized in colour on a monitor. This visual image graphically maps the body temperature and is referred to as a thermogram. The spectrum of colours indicate an increase or decrease in the amount of infrared radiation being emitted from the body surface. Since there is a high degree of thermal symmetry in the normal body, subtle abnormal temperature asymmetry's can be easily identified.

Clinical studies show that thermal imaging of the breasts has an average sensitivity and specificity of 90%. An abnormal infrared image is the single most important marker of high risk for developing breast cancer. Thermal imaging can be used

(i) to define the extent of a lesion of which a diagnosis has previously been made;

(ii) to localize an abnormal area not previously identified, so further diagnostic tests can be performed;

(iii) to detect early lesions before they are clinically evident;

(iv) to guide thermal ablation therapies.

Ultrasonic temperature imaging is a promising technique using thermography. It exploits the principle that the sound speed in tissue depends on temperature. Thermal ablation

therapies, such as focused ultrasound surgery, aim to destroy malignant tumors without damaging the surrounding tissue. The technique is to run the focused ultrasound surgery system at an initial, pre-ablative low intensity and to use a diagnostic ultrasound imaging system to detect the associated localized temperature rise, assuming that the temperature dependence of speed of sound is known.

Electrical Impedance Endo-Tomography (EIET) is a new alternative method for scanning the conductivity of deep tissues or organs using an impedance probe placed at the center of the region of interest. The probe consists of electrodes placed at the surface of an insulating cylinder and spreads in the medium surrounding the probe. The electrodes are surrounded by the medium to be examined instead of encircling it. The basic assumption is that normal prostate tissue and tumor tissue have different electric conductivities.

In practice captured current-voltage pairs must be limited by the number of electrodes attached on the surface of the probe, that restrict the resolution of the image. Definitely, we can increase the resolution of the conductivity image by increasing the number of electrodes. However, it should be noticed that, beyond a certain level, increasing numbers of electrodes may not give any help for producing a better image for the inner-region of the body if we take account of inevitable noise in measurements and the inherent insensitivity mentioned before. In its most general form EIET is severely ill-posed and nonlinear. These major and fundamental difficulties can be understood by means of the mean value type theorem in elliptic partial differential equations. The value of the voltage potential at each point in the medium surrounding the probe can be expressed as a weighted average of its neighborhood potential where the weight is determined by the conductivity distribution. In this weighted averaging way, the conductivity distribution is conveyed to the probe potential. Therefore, the probe data is entangled in the global structure of the conductivity distribution in a highly nonlinear way. This is the main obstacle in finding non-iterative reconstruction algorithms with limited data. If, however, we have additional structural information about the medium in advance, then we may be able to determine specific features about the conductivity distribution with good resolution. One such type of knowledge could be that the body surrounding the probe consists of a smooth background containing a number of unknown small inclusions with a significantly different conductivity. This situation arises for example in prostate cancer imaging.

In this case, EIET tries to recover the unknown inclusions. Due to the smallness of the inclusions the associated voltage potentials measured on the surface of the probe are very close to the potentials corresponding to the medium without inclusion. Thus unless one knows exactly what patterns to look for, noise will largely dominate the information contained in the measured data. Furthermore, in prostate imaging it is often not necessary to reconstruct the precise values of the conductivity or geometry of the inclusions. The information of real interest is their positions and size.

Thesis outline

The thesis is organized as follows.

In Chapter 1, we provide the mathematical basis for the three different magneto-acoustic imaging approaches and propose new algorithms for solving the inverse problem for each of them.

Chapter 2 is devoted to the thermographic imaging. We perform a quantitative study of the change of temperature due to a small anomaly and design new accurate algorithms for localizing and estimating the size of the anomaly. We adopt a model that can be viewed essentially as a realistic, therefore any developed theory from this model can be applied to other areas in thermography, especially in anomaly detection problems. Our purpose is to provide a mathematical ground for the reconstruction of a rough feature of the anomaly which is stable against any measurement noise and any change of geometry. Based on rigorous estimates, we derive an approximation that gives a noniterative detection algorithm of finding a useful feature of anomaly. We also provide the mathematical ground of ultrasonic temperature imaging used for the guidance of thermal ablation therapies.

In Chapter 3, we study electrical impedance endo-tomography. Our aim is threefold:

(i) We first find an isotropic inclusion of elliptic form with isotropic conductivity first-order polarization tensor of which coincides with the anisotropic one of a disk-shaped anisotropic inclusion. We then show how to extract anisotropy from higher-order anisotropic polarization tensors. It is known that detection of anisotropy can discriminate malignant tumors from benign ones.

(ii) We also generalize the recent approach of conductivity imaging by elastic deformation to EIET and demonstrate its feasibility. This approach, called impediography, is based on the simultaneous measurement of a potential and of acoustic vibrations induced by ultrasound waves. Its intrinsic resolution depends on the size of the focal spot of the acoustic perturbation, and thus it provides high resolution images. The core idea of impediography is to extract more information about the conductivity from data that has been enriched by coupling the electric measurements with localized elastic perturbations. More precisely, one perturbs the medium during the electric measurements, by focusing ultrasonic waves on regions of small diameter inside the body. Using a simple model for the mechanical effects of the ultrasound waves, one can show that the difference between the measurements in the unperturbed and perturbed configurations is asymptotically equal to the pointwise value of the energy density at the center of the perturbed zone. In practice, the ultrasounds impact a zone of a few millimeters in diameter. The perturbation should thus be sensitive to conductivity variations at the millimeter scale, which is the precision required for prostate cancer diagnostic.

(iii) Finally, we present a method for detecting multiple anomalies using a realistic electrode model.

Chapter 1

Mathematical Models and Reconstruction Methods in Magneto-Acoustic Imaging

1.1 Introduction

In magneto-acoustic imaging, a probe signal such as an acoustic wave or an electric current (or voltage) is applied to a biological tissue placed in a magnetic field. The probe signal produces by the Lorentz force an induced signal that is a function of the local electrical conductivity of the biological tissue [33]. If the probe signal is an acoustic wave, then the induced signal is an electric current and the Lorentz force causes a local current density.

Induced boundary currents (a) or pressure (b) which are proportional to the local electrical conductivity can be measured to reconstruct the conductivity distribution with the spatial resolution of the ultrasound. The induced signal is detected and an image of the local electrical conductivity of the specimen is generated based on the detected induced signal. Method (a) is referred as the vibration potential imaging and method (b) as magneto-acoustic tomography with magnetic induction. The vibration potential imaging is also known as the Hall effect imaging.

Method (a) can be applied to body tissue *in vivo* and to measurements in suspensions and cultured cells. The ultrasound beam ensures the excitation of the desired region of interest and the interaction current is collected by means of electrodes. It is a very promising direction of research for improving the electrical impedance tomography (EIT). EIT is an imaging technique focused upon reconstructing the impedance distribution of biological tissue using current injection and noninvasive voltage measurements. In EIT, electrical current is injected into the object from electrodes attached to the surface, and the corresponding boundary voltage is measured over the surface of the object in order to reconstruct the impedance distribution within the volume. It is known that this approach for imaging the conductivity distribution produces images with deceivingly poor accuracy

and spatial resolution. The vibration potential imaging relies on innovative measurement techniques that incorporate structural information. Its intrinsic resolution is of order of the size of the focal spot of the ultrasound, and thus it should provide high resolution images.

If an electrically active tissue is placed on a magnetic field then an acoustic wave or tissue displacement is created. This method (c), known as magneto-acoustic current imaging, has been suggested as a method for reconstructing current dipoles and imaging action currents arising from active nerve or muscle fibers by detecting the induced pressure signal.

We refer the reader to [33, 27, 28, 39, 40, 17, 35, 36] for physical basic principles of vibration potential tomography, magneto-acoustic tomography with magnetic induction, and magneto-acoustic current imaging.

In this chapter, we provide the mathematical basis for these three different magneto-acoustic imaging approaches and propose new algorithms for solving the inverse problem for each of them.

1.2 Mathematical Formulations

1.2.1 Vibration Potential Tomography

We recall that, in mathematical terms, EIT consists in recovering the conductivity map of a 2D or 3D body Ω (of class $\mathcal{C}^{1,\alpha}, \alpha > 0$), from one or several current-to-voltage pairs measured on the surface of the body. Denoting by $\gamma(x)$ the unknown conductivity, the voltage potential v solves the conduction problem

$$\begin{cases} \nabla \cdot (\gamma \nabla v) = 0 & \text{in } \Omega, \\ v = g & \text{on } \partial\Omega. \end{cases} \tag{1.1}$$

The problem of impedance tomography is the inverse problem of recovering the coefficients γ of the elliptic conduction partial differential equation, knowing one or more current-to-voltage pairs $\left(g, \frac{\partial v}{\partial \nu}|_{\partial\Omega}\right)$. Throughout this chapter, except in Section 1.4, we assume that $g \in \mathcal{C}^{1,\alpha}(\overline{\Omega})$ and the conductivity $\gamma \in \mathcal{C}^{0,\alpha}(\overline{\Omega})$, and is bounded in Ω above and below by positive constants. The solution v is then in $\mathcal{C}^{1,\alpha}(\overline{\Omega})$. Further, we suppose that the γ *is a known constant on a neighborhood of the boundary* $\partial\Omega$ and let γ_* denote $\gamma|_{\partial\Omega}$.

In vibration potential tomography (VPT), ultrasonic waves are focused on regions of small diameter inside a body placed on a static magnetic field. The oscillation of each small region results in frictional forces being applied to the ions, making them move. In the presence of a magnetic field, the ions experience Lorentz force. This gives rise to a localized current density within the medium. The current density is proportional to the local electrical conductivity [33]. In practice, the ultrasounds impact a spherical or ellipsoidal zone, of a few millimeters in diameter. The induced current density should

thus be sensitive to conductivity variations at the millimeter scale, which is the precision required for breast cancer diagnostic. The feasibility of this conductivity imaging technique has been demonstrated in [14].

Let $z \in \Omega$ and D be a small impact zone around the point z. The created current by the Lorentz force density is given by

$$\mathbf{J}_z(x) = c\chi_D(x)\gamma(x)\mathbf{e}, \tag{1.2}$$

for some constant c and a constant unit vector $\mathbf{e}$ both of which are independent of z. Here and throughout this chapter, χ_D denotes the characteristic function of D. With the induced current $\mathbf{J}_z$ the new voltage potential, denoted by u_z, satisfies

$$\begin{cases} \nabla \cdot (\gamma \nabla u_z + \mathbf{J}_z) = 0 \quad \text{in } \Omega, \\ u_z = g \quad \text{on } \partial\Omega. \end{cases}$$

According to (1.2), the induced electrical potential $w_z := v - u_z$ satisfies the conductivity equation:

$$\begin{cases} \nabla \cdot (\gamma \nabla w_z) = c\nabla \cdot (\chi_D \gamma \mathbf{e}) \quad \text{for } x \in \Omega, \\ w_z(x) = 0 \quad \text{for } x \in \partial\Omega. \end{cases} \tag{1.3}$$

The inverse problem for the vibration potential tomography is to reconstruct the conductivity profile γ from boundary measurements of $\frac{\partial u_z}{\partial \nu}|_{\partial\Omega}$ or equivalently $\frac{\partial w_z}{\partial \nu}|_{\partial\Omega}$ for $z \in \Omega$.

Throughout this chapter, we assume that γ is constant in D. This assumption is natural since the resolution can not be lower than the characteristic size of the ultrasonic beam. Recall that γ is known in a neighborhood of the boundary $\partial\Omega$.

Let $|D|$ denote the volume of D. Since γ is assumed to be constant in D and $|D|$ is small, we obtain using Green's identity

$$\begin{aligned} \int_{\partial\Omega} \gamma_* \frac{\partial w_z}{\partial \nu} g d\sigma &= \int_\Omega \nabla \cdot (\gamma \nabla w_z) v dx \\ &= c \int_\Omega \nabla \cdot (\chi_D \gamma \mathbf{e}) v dx \\ &= -c \int_D \gamma \mathbf{e} \cdot \nabla v dx = -c \int_D \mathbf{e} \cdot \nabla(\gamma v) dx \\ &\approx -c|D| \nabla(\gamma v)(z) \cdot \mathbf{e}. \end{aligned} \tag{1.4}$$

Note that the approximation error in (1.4) is

$$c\gamma(z) \int_D \mathbf{e} \cdot [\nabla v(x) - \nabla v(z)]\, dx,$$

and it is $o(|D|)$ as one can easily prove using the Lebesgue Theorem. Here, the regularity of the gradient ∇v is used. Truly, only a *local* regularity of the gradient around D is required.

Regularity does not affect the reconstruction procedures presented in Section 1.3.1. In fact, in Section 1.4 we consider discontinuous conductivities. The approximation is only used for the derivation of formula 1.4. When the measurement is taken at a location D where the conductivity is irregular, this formula is not accurate. However, as it is shown in Section 1.3 and Section 1.4, the reconstruction is essentially local, and no spatial diffusion of the error occurs. This approximation simply tend to slightly smooth the jumps of the conductivity.

The relation (1.4) shows that, by scanning the interior of the body with ultrasound waves, $c\nabla(\gamma v)(z)\cdot\mathbf{e}$ can be computed from the boundary measurements $\frac{\partial w_z}{\partial\nu}|_{\partial\Omega}$ in Ω. If we can rotate the subject, then $c\nabla(\gamma v)(z)$ for any z in Ω can be reconstructed. In practice, the constant c is not known. But, since γv and $\frac{\partial(\gamma v)}{\partial\nu}$ on the boundary of Ω are known, we can recover c and γv from $c\nabla(\gamma v)$ in a constructive way. To see this, let us put

$$u := \gamma v, \quad h := c\nabla(\gamma v), \quad \varphi := (\gamma v)|_{\partial\Omega}, \quad \psi := \frac{\partial(\gamma v)}{\partial\nu}\Big|_{\partial\Omega}.$$

Note that h, φ and ψ are known. The new unknown u satisfies

$$\begin{cases} c\Delta u = \nabla\cdot h \quad \text{in } \Omega, \\ u|_{\partial\Omega} = \varphi, \\ \dfrac{\partial u}{\partial\nu}\Big|_{\partial\Omega} = \psi. \end{cases} \tag{1.5}$$

Thus, if c can be evaluated, we can reconstruct u, using either of the boundary data. Let us define

$$w(x) := \int_\Omega \Gamma(x-y)\nabla\cdot h(y)\,dy, \quad x\in\Omega,$$

where $\Gamma(x)$ is the fundamental solution of the Laplacian in $\mathbb{R}^d$, then $cu - w$ satisfies

$$\begin{cases} \Delta(cu-w) = 0 \quad \text{in } \Omega, \\ (cu-w)|_{\partial\Omega} = c\varphi - w|_{\partial\Omega}, \\ \dfrac{\partial(cu-w)}{\partial\nu}\Big|_{\partial\Omega} = c\psi - \dfrac{\partial w}{\partial\nu}\Big|_{\partial\Omega}. \end{cases} \tag{1.6}$$

Let us now define Λ as the Dirichlet-to-Neumann map for the Laplacian. Then, (1.6) implies that

$$\Lambda(c\varphi - w|_{\partial\Omega}) = c\psi - \frac{\partial w}{\partial\nu}\Big|_{\partial\Omega},$$

and therefore

$$c\big(\Lambda(\varphi)-\psi\big) = \Lambda(w|_{\partial\Omega}) - \frac{\partial w}{\partial\nu}\Big|_{\partial\Omega}. \tag{1.7}$$

Since everything but c is known in (1.7), this gives the value of c provided this identity is not trivial. Let us now address this point. Note that because γ is constant in a neighborhood of $\partial\Omega$, $\nabla\cdot h$ is compactly supported in Ω. If $\Lambda(\varphi)-\psi\equiv 0$ then $\nabla\cdot h$ is

orthogonal to any harmonic function in Ω and therefore it is naught almost everywhere by the density of harmonic functions in $L^2(\Omega)$. This means that either c is zero, or $v \equiv 0$ in Ω. Thus provided that the imposed boundary potential $g \neq 0$, we have proved that c can be computed using (1.7) and, in turn, u using the first two equations in (1.5). We emphasize that Λ can be computed easily. In fact, it is the normal derivative of the Poisson integral.

The new inverse problem is now to reconstruct the contrast profile γ knowing

$$\mathcal{E}(z) := \gamma(z)v(z)$$

for a given boundary potential g, where v is the solution to (1.1).

1.2.2 Magneto-Acoustic Tomography with Magnetic Induction

In the magneto-acoustic tomography with magnetic induction (MAT-MI), pulsed magnetic stimulation by the ultrasound beam is imposed on an object placed in a static magnetic field. The magnetic stimulation can be considered as an ideal pulsed distribution over time. The magnetically induced eddy current is then subject to Lorentz force. This in turn creates a pressure wave that can be detected using an ultrasound hydrophone [33]. The MAT-MI uses this acoustic pressure wave to reconstruct the conductivity distribution of the sample as the focus of the ultrasound beam scans the entire domain.

Let γ be the conductivity distribution of the specimen. Denoting the constant magnetic field as B_0 and the magnetically induced current density distribution as $\mathbf{J}_z(x)$ with z indicating the location of the magnetic stimulation, the Lorentz force is given by

$$\mathbf{J}_z(x) \times B_0\delta_{t=0} = c\chi_D\gamma\mathbf{e}\delta_{t=0},$$

where D is the impact zone which is a small neighborhood of z as before, and c is a constant independent of z and x. Then the wave equation governing the pressure distribution p_z can be written as

$$\frac{\partial^2 p_z}{\partial t^2} - c_s^2\Delta p_z = 0, \quad x \in \Omega, \quad t \in]0, T[, \tag{1.8}$$

for some final observation time T, where c_s is the acoustic speed in Ω. The pressure satisfies the Dirichlet boundary condition

$$p_z = 0 \quad \text{on } \partial\Omega\times]0, T[\tag{1.9}$$

and the initial conditions

$$p_z|_{t=0} = 0 \quad \text{and} \quad \frac{\partial p_z}{\partial t}\Big|_{t=0} = -c\nabla\cdot(\chi_D\gamma\mathbf{e}) \quad \text{in } \Omega. \tag{1.10}$$

The inverse problem for the MAT-MI is to determine the conductivity distribution γ in Ω from boundary measurements of $\frac{\partial p_z}{\partial \nu}$ on $\partial\Omega\times]0, T[$ for all $z \in \Omega$. We will assume that T is large enough so that

$$T > \frac{\text{diam}(\Omega)}{c_s}. \tag{1.11}$$

It says that the observation time is long enough for the wave initiated at z to reach the boundary $\partial\Omega$.

1.2.3 Magneto-Acoustic Current Imaging

Similarly to MAT-MI, it is possible to detect a pressure signal created in the presence of a magnetic field by electrically active tissues [17, 35, 36]. A magneto-acoustic technique has been developed to image electrical activity in biological tissue. In the presence of an externally applied magnetic field, biological action currents, arising from active nerve or muscle fibers, experience a Lorentz force. The resulting pressure or tissue displacement contains information about the action current distribution.

Let $z \in \Omega$ be the location of an electric dipole, which represents an active nerve or muscle fiber, with strength c. The wave equation governing the induced pressure distribution p_z can be written as

$$\frac{\partial^2 p_z}{\partial t^2} - c_s^2 \Delta_x p_z = 0, \quad x \in \Omega, \quad t \in]0, T[, \tag{1.12}$$

for some final observation time T, where c_s is the acoustic speed in Ω. The pressure satisfies the Dirichlet boundary condition (1.9) and the initial conditions (1.10).

The inverse problem for the magneto-acoustic current imaging is to reconstruct the position z and the strength c of the dipole from boundary measurements of $\frac{\partial p_z}{\partial \nu}$ on $\partial\Omega \times]0, T[$. So this problem is to find an active nerve or muscle fiber from boundary measurements of the wave. Here again we assume the final observation time T is large enough so that (1.11) holds.

1.3 Reconstruction Methods

1.3.1 Reconstruction Methods for the VPT

Recall that the inverse problem for the VPT is to reconstruct the conductivity distribution γ from the quantity $\mathcal{E}(z)$, $z \in \Omega$, which can be computed from the boundary measurements $\frac{\partial v_z}{\partial \nu}|_{\partial\Omega}$, where v_z is the solution to (1.3). The relation between γ and $\mathcal{E}(z)$ is approximately given by

$$\gamma(z) = \frac{\mathcal{E}(z)}{v(z)}, \tag{1.13}$$

where v is the solution to (1.1).

In view of (1.13), v satisfies

$$\begin{cases} \nabla \cdot \left(\dfrac{\mathcal{E}}{v} \nabla v \right) = 0 & \text{in } \Omega, \\ v = g & \text{on } \partial\Omega. \end{cases} \tag{1.14}$$

If we solve (1.14) for v, then (1.13) yields the conductivity contrast γ. Note that to be able to solve (1.14) we need to know the coefficient $\mathcal{E}(z)$ for all z, which amounts to scanning

all the points $z \in \Omega$ by the ultrasonic beam. It is quite interesting to compare VPT with MAT-MI in this respect and we will address this point at the end of the next subsection.

Observe that solving (1.14) is quite easy mathematically: If we put $w = \ln v$, then w is the solution to

$$\begin{cases} \nabla \cdot (\mathcal{E} \nabla w) = 0 \quad \text{in } \Omega, \\ w = \ln g \quad \text{on } \partial\Omega, \end{cases} \tag{1.15}$$

as long as $g \geq 0$. Thus if we solve (1.15) for w, the $v = e^w$ is the solution to (1.14). However, taking exponent may amplify the error which already exists in the computed data $\mathcal{E}$. See Section 1.4 for the numerical examples. In order to avoid this numerical instability, we solve (1.14) iteratively. We note that the argument in this paragraph ensures the existence and uniqueness of the solution to (1.14) as long as $\ln g \in H^{1/2}(\partial\Omega)$.

To solve (1.14) we adopt an iterative scheme similar to the one proposed in [3]. Start with γ_0 and let v_0 be the solution of

$$\begin{cases} \nabla \cdot \gamma_0 \nabla v_0 = 0 \quad \text{in } \Omega, \\ v_0 = g \quad \text{on } \partial\Omega. \end{cases} \tag{1.16}$$

According to (1.13), our updates, $\gamma_0 + \delta\gamma$ and $v_0 + \delta v$, should satisfy

$$\gamma_0 + \delta\gamma = \frac{\mathcal{E}}{v_0 + \delta v}, \tag{1.17}$$

where

$$\begin{cases} \nabla \cdot (\gamma_0 + \delta\gamma) \nabla (v_0 + \delta v) = 0 \quad \text{in } \Omega, \\ \delta v = 0 \quad \text{on } \partial\Omega, \end{cases}$$

or

$$\begin{cases} \nabla \cdot \gamma_0 \nabla \delta v + \nabla \cdot \delta\gamma \nabla v_0 = 0 \quad \text{in } \Omega, \\ \delta v = 0 \quad \text{on } \partial\Omega. \end{cases} \tag{1.18}$$

We then linearize (1.17) to have

$$\gamma_0 + \delta\gamma = \frac{\mathcal{E}}{v_0(1 + \delta v / v_0)} \approx \frac{\mathcal{E}}{v_0} \left(1 - \frac{\delta v}{v_0}\right). \tag{1.19}$$

Thus

$$\delta\gamma = -\frac{\mathcal{E}\delta v}{v_0^2} - \delta, \quad \delta = -\frac{\mathcal{E}}{v_0} + \gamma_0. \tag{1.20}$$

We then find δv by solving

$$\begin{cases} \nabla \cdot \gamma_0 \nabla \delta v - \nabla \cdot \left(\frac{\mathcal{E}\delta v}{v_0^2} + \delta \right) \nabla v_0 = 0 \quad \text{in } \Omega, \\ \delta v = 0 \quad \text{on } \partial\Omega. \end{cases}$$

or equivalently

$$\begin{cases} \nabla \cdot \gamma_0 \nabla \delta v - \nabla \cdot \left(\frac{\mathcal{E} \nabla v_0}{v_0^2} \delta v \right) = \nabla \cdot \delta \nabla v_0 \quad \text{in } \Omega, \\ \delta v = 0 \quad \text{on } \partial\Omega. \end{cases} \tag{1.21}$$

Our reconstruction procedure is as follows.

[**Iterative Reconstruction Procedure**]:

1. Start with an initial guess γ_0 for the conductivity contrast.
2. Solve (1.16) to obtain v_0.
3. Compute $\delta = -\frac{\mathcal{E}}{v_0} + \gamma_0$.
4. Solve (1.21) to obtain δv.
5. Compute $\delta\gamma = -\dfrac{\mathcal{E}\delta v}{v_0^2} - \delta$.
6. Replace γ_0 by $\gamma_0 + \delta\gamma$.

In the case of incomplete data, that is, if $\mathcal{E}$ is only known on a subset Ω of the domain, we can follow an optimal control approach as used in [12]. We minimize the functional

$$\mathcal{J}(\sigma) = \int_\Omega \chi_\Omega \left(\gamma - \frac{\mathcal{E}}{v} \right)^2 \tag{1.22}$$

over all $\gamma = \exp(\sigma)$ with $\sigma \in L^\infty(\Omega)$ and $\gamma = \gamma^*$ in a neighborhood D of $\partial\Omega$, where χ_Ω is the characteristic function of Ω, and v is the solution of (1.1). Note that $\mathcal{J}$ depends on σ analytically. The derivative of $\mathcal{J}$ with respect to σ applied to $\delta \in L^\infty(\Omega)$ is

$$D\mathcal{J}(\sigma) \cdot \delta = 2 \int_\Omega \left(\delta\gamma + v_\delta \frac{1}{v^2} \mathcal{E} \right) \left(\gamma - \frac{\mathcal{E}}{v} \right),$$

where $v_\delta \in H_0^1(\Omega)$ is the solution of

$$\nabla \cdot (\gamma \nabla v_\delta) + \nabla \cdot (\delta\gamma \nabla v) = 0 \quad \text{in } \Omega.$$

Let $w \in H_0^1(\Omega)$ be the solution of the adjoint problem

$$\nabla \cdot \gamma \nabla w = \chi_\Omega \frac{1}{v^2} \mathcal{E} \left(\gamma - \frac{\mathcal{E}}{v} \right) \quad \text{in } \Omega,$$

After integrations by parts, we see that the derivative of $\mathcal{J}$ can be written

$$D\mathcal{J}(\sigma) \cdot \delta = 2 \int_\Omega \delta\gamma \left(\chi_\Omega \left(\gamma - \frac{\mathcal{E}}{v} \right) + \nabla w \cdot \nabla v \right).$$

Therefore, choosing δ of the form

$$\delta = -\frac{1}{2\gamma} \left(\chi_\Omega \left(\gamma - \frac{\mathcal{E}}{v} \right) + \nabla w \cdot \nabla v \right), \tag{1.23}$$

we obtain

$$D\mathcal{J}(\sigma)\cdot\delta = -\int_\Omega \gamma\left(\chi_\Omega\left(\gamma - \frac{\mathcal{E}}{v}\right) + \nabla w\cdot\nabla v\right)^2 \leq 0. \tag{1.24}$$

[**Optimal Control Reconstruction Procedure**]:

1. Starting from an arbitrary γ for the conductivity and an arbitrary stepsize h.
2. Compute $\tilde{\gamma} := \gamma(1 + h\delta)$, where δ is given by (1.23).

3a. If $\mathcal{J}(\tilde{\sigma}) < \mathcal{J}(\sigma)$, we set $\gamma := \tilde{\gamma}$ and increase the step size h.

3b. If $\mathcal{J}(\tilde{\sigma}) > \mathcal{J}(\sigma)$, decrease the stepsize h and return to Step 2 (as we know from (1.24) that for sufficiently small h, the objective $\mathcal{J}$ does not increase).

4 Repeat Steps 1, 2 and 3 until $\mathcal{J}$ is small enough.

Note that the optimal control procedure can also be applied to the case of complete data. The procedure described before is simpler than the optimal control procedure in the sense that it does not require the determination of a stepsize. However, the optimal control approach has the advantage of embedded stability, as it is a minimization procedure.

It is also worth emphasizing that both reconstruction procedures work well for discontinuous conductivities because of their local character.

1.3.2 Reconstruction Method for the MAT-MI

The algorithms for the MAT-MI available in the literature are limited to unbounded media. They use the Spherical Radon transform inversion. However, the pressure field is significantly affected by the acoustic boundary conditions at the tissue-air interface, where the pressure must vanish. Thus, we cannot base magneto-acoustic imaging on pressure measurements made over a free surface. Instead, we propose the following algorithm.

Let v satisfy

$$\frac{\partial^2 v}{\partial t^2} - c_s^2\Delta v = 0 \quad \text{in } \Omega\times]0,T[, \tag{1.25}$$

with the final conditions

$$v|_{t=T} = \frac{\partial v}{\partial t}\Big|_{t=T} = 0 \quad \text{in } \Omega. \tag{1.26}$$

Multiply both sides of (1.8) by v and integrate them over $\Omega\times[0,T]$. Since γ is constant on D then after some integrations by parts this leads to the following identity:

$$\int_0^T\int_{\partial\Omega}\frac{\partial p_z}{\partial\nu}(x,t)v(x,t)\,d\sigma(x)\,dt = \frac{c\gamma(z)}{c_s^2}\int_D \mathbf{e}\cdot\nabla v(x,0)dx. \tag{1.27}$$

As before we assume that γ is constant D which is reasonable as D is small. Suppose that $d = 3$. For $y \in \mathbb{R}^3 \setminus \overline{\Omega}$, let

$$v_y(x,t) := \frac{\delta\left(t + \tau - \frac{|x-y|}{c_s}\right)}{4\pi|x-y|} \quad \text{in } \Omega\times]0,T[, \tag{1.28}$$

where δ is the Dirac mass at 0 and $\tau := \frac{|y-z|}{c_s}$. It is easy to check that v_y satisfies (1.25) (see e.g. [13, page 117]). Moreover, since

$$|y-z| - |x-y| \le |x-z| \le \mathrm{diam}(\Omega)$$

for all $x \in \Omega$, v_y satisfies (1.26) provided that the condition (1.11) is fulfilled. Choosing v_y as a test function in (1.27) and obtain the new identity

$$c\gamma(z) = \frac{c_s^2}{\int_D \mathbf{e}\cdot\nabla v_y(x,0)dx}\int_0^T\int_{\partial\Omega}\frac{\partial p_z}{\partial\nu}(x,t)v_y(x,t)\,d\sigma(x)\,dt. \tag{1.29}$$

Let us now compute $\int_D \mathbf{e}\cdot\nabla v_y(x,0)dx$. Note that, in a distributional sense,

$$\nabla v_y(x,0) = \delta\left(\tau - \frac{|x-y|}{c_s}\right)\frac{y-x}{4\pi|x-y|^3} + \delta'\left(\tau - \frac{|x-y|}{c_s}\right)\frac{y-x}{4\pi c_s|x-y|^2}. \tag{1.30}$$

Thus we have

$$\begin{aligned}\int_D \mathbf{e}\cdot\nabla v_y(x,0)dx &= \int_D \frac{(y-x)\cdot\mathbf{e}}{4\pi|x-y|^3}\,\delta\left(\tau - \frac{|x-y|}{c_s}\right)dx \\ &\quad + \int_D \frac{(y-x)\cdot\mathbf{e}}{4\pi c_s|x-y|^2}\,\delta'\left(\tau - \frac{|x-y|}{c_s}\right)dx \\ &:= I + II.\end{aligned}$$

Letting $s = |x-y|$ and $\sigma = \frac{x-y}{|x-y|}$, we have by a change of variables ($t = \tau - s/c - s$)

$$\begin{aligned}I &= -\frac{1}{4\pi}\int_0^\infty\int_{S^2}\chi_D(s\sigma+y)(\sigma\cdot\mathbf{e})\,\delta\left(\tau - \frac{s}{c_s}\right)d\sigma\,ds \\ &= -\frac{c_s}{4\pi}\int_{S^2}\chi_D(c_s\tau\sigma+y)(\sigma\cdot\mathbf{e})\,d\sigma,\end{aligned}$$

where S^2 is the unit sphere. Since $c_s\tau = |y-z|$, we have

$$I = -c_s A_D(0), \tag{1.31}$$

where $A_D(t)$, $t \in \mathbb{R}^1$, is defined by

$$A_D(t) := \frac{1}{4\pi}\int_{S^2}\chi_D((|z-y|-t)\sigma+y)(\sigma\cdot\mathbf{e})\,d\sigma. \tag{1.32}$$

We now compute II. Using the same polar coordinates s and σ centered at y, we have

$$II = -\frac{1}{4\pi c_s}\int_0^\infty s\int_{S^2}\chi_D(s\sigma+y)(\sigma\cdot\mathbf{e})\,\delta'\left(\tau-\frac{s}{c_s}\right)d\sigma\,ds,$$

and hence

$$\begin{aligned} II &= -\frac{c_s}{4\pi}\frac{d}{dt}\left[(\tau-t)\int_{S^2}\chi_D(c_s(\tau-t)\sigma+y)(\sigma\cdot\mathbf{e})\,d\sigma\right]_{t=0} \\ &= \frac{c_s}{4\pi}\int_{S^2}\chi_D(|z-y|\sigma+y)(\sigma\cdot\mathbf{e})\,d\sigma - \frac{c_s\tau}{4\pi}\frac{d}{dt}\left[\int_{S^2}\chi_D(c_s(\tau-t)\sigma+y)(\sigma\cdot\mathbf{e})\,d\sigma\right]_{t=0} \end{aligned}$$

Thus, we have

$$II = c_sA_D(0) - c_s|z-y|A_D'(0). \tag{1.33}$$

Combining (1.31) and (1.33) we obtain

$$\int_D \mathbf{e}\cdot\nabla v_y(x,0)dx = -c_s|z-y|A_D'(0), \tag{1.34}$$

and hence

$$c\gamma(z) = -\frac{c_s}{|z-y|A_D'(0)}\int_0^T\int_{\partial\Omega}\frac{\partial p_z}{\partial\nu}(x,t)v_y(x,t)\,d\sigma(x)\,dt. \tag{1.35}$$

Note that the function $A_D(t)$ is dependent on the shape of D and the direction $\mathbf{e}$, and it is not likely to be able to compute it in a close form. But, if we take the source point y so that $z-y$ is parallel to $\mathbf{e}$ and D is a sphere of radius r (its center is z), then one can compute $A_D(t)$ explicitly using the spherical coordinates. In fact, in such a case, we have

$$A_D(t) = \frac{r^2}{4(|z-y|-t)^2} - \frac{r^4}{16(|z-y|-t)^4}, \tag{1.36}$$

and hence we obtain a formula for the reconstruction of $c\gamma(z)$ from (1.35). Let us summarize the formula in the following theorem

Theorem 1.3.1 *Choose $y\in\mathbb{R}^3\setminus\Omega$ so that $z-y$ is parallel to $\mathbf{e}$. If D is a sphere of radius r with its center at z, then*

$$c\gamma(z) = -\frac{c_s}{\frac{r^2}{2|z-y|^2}-\frac{r^4}{4|z-y|^4}}\int_0^T\int_{\partial\Omega}\frac{\partial p_z}{\partial\nu}(x,t)v_y(x,t)\,d\sigma(x)\,dt. \tag{1.37}$$

provided that γ is constant $\gamma(z)$ on D.

Note that the formula (1.37) is an exact formula. But since r is sufficiently small and we are using approximation $\gamma\approx\gamma(x)$ on D, it is preferable to use the following approximate formula.

[**Reconstruction Formula for MAT-MI**]

$$c\gamma(z) \approx -\frac{2c_s|z-y|^2}{r^2}\int_0^T\int_{\partial\Omega}\frac{\partial p_z}{\partial\nu}(x,t)v_y(x,t)\,d\sigma(x)\,dt \tag{1.38}$$

If the impact zone D is the sphere of radius r centered at z and y is chosen so that $z-y$ is parallel to $\mathbf{e}$.

Formula (1.38) can be used to effectively compute the conductivity contrast in Ω with a resolution of order the size of the ultrasound beam.

It is worth mentioning that in order to obtain $c\gamma(z)$ using the MAT-MI, it suffices to stimulate the point z, while for the VPT we need to stimulate all the points in the body even if we want to detect the conductivity of a local region. This is due to difference between the nature of differential equations involved: finite speed of propagation of the wave equation (MAT-MI) and infinite speed of the elliptic equation (VPT).

1.3.3 Localization Method for the MACI

Let Σ be a plane in $\mathbb{R}^3\setminus\overline{\Omega}$ orthogonal to $\mathbf{e}$. Let v_y be given by (1.28), where $y\in\Sigma$. We have by multiplying (1.12) by v_y and integrating by parts that

$$\mathcal{E}(y) := \int_0^T\int_{\partial\Omega}\frac{\partial p_z}{\partial\nu}(x,t)v_y(x,t)\,d\sigma(x)\,dt = c\frac{(y-z)\cdot\mathbf{e}}{4\pi|z-y|^3}. \tag{1.39}$$

The projection on Σ of the location z can be obtained by taking the maximum of $\mathcal{E}(y)$ as $y\in\Sigma$. The third component of z can be obtained as the point on a line parallel to $\mathbf{e}$ where $\mathcal{E}(y)$ changes sign. This algorithm is parallel to the one developed in [25] for anomaly detection from electrical impedance boundary measurements.

1.4 Examples of Applications

1.4.1 Vibration Potential Tomography with FreeFem++

We present a test for iterative procedures proposed for the VPT reconstruction. The domain Ω is the disk of radius 6 centered at the origin. Next to the boundary, that is, outside of a disk of radius 5, the conductivity is constant, equal to 1. In the region of the radius 5, the background conductivity is an oscillating function, $\sin\left(4\sqrt{x^2+y^2}\right)+2$. We introduced three zones where the conductivity is notably different: An area with an irregular boundary where the conductivity is a piecewise constant function $\text{int}\,(8/10\cos(4y)+9/10)+1/10$, where int is the integer part function, a small stretched ellipse with constant conductivity $1/10$, and an annulus where the conductivity increases rapidly $(x+2)^2+0.1$. The purpose of choosing this pattern is to demonstrate that the reconstruction methods are very

effective for a large variety of conductivities. The conductivity distribution is presented on the Figure 1.1. The simulations are done using the partial differential equation solver FreeFem++ [15].

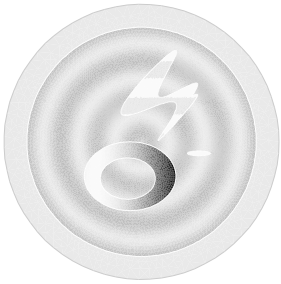

Figure 1.1: Conductivity Distribution.

Figure 1.2 shows the result of the reconstruction when perfect measurements (with 'infinite' precisions) are available. We use two different Dirichlet boundary data, $g_x = 2 + x/6$ and $g_y = 2 + y/6$. In the first approach proposed in Section 1.3.1, this is implemented by alternating the procedures with g_x and g_y. In the optimal control approach, this corresponds to simply adding the contribution of both correctors. In both cases, the boundary data are positive, which implies the positivity of u in the domain Ω. The initial guess is depicted on the left: it is equal to 1 everywhere. The right picture represents the reconstructed conductivity after three iterations. A 7 digit accuracy in L^2 norm and in L^∞ norm is reached after five iterations.

Figure 1.2: Perfect reconstruction test. From left to right, the initial guess, the reconstructed conductivity after three iterations

To document the effectiveness of our approach in the case of partial data, we perturb the measure data. We add 5% noise to the measured data, and we destroy the data on two elliptical subdomains, replacing it by 1. If we use solve iteratively, using alternatively the (perturbed) data corresponding to g_x or g_y, the algorithm cycles after fives iterations. This is because we are trying to match mismatched data : the minimum corresponding to g_x data is not the same as the one corresponding to g_y, because of the perturbations we applied to both data sets. The results are presented in Figure 1.3.

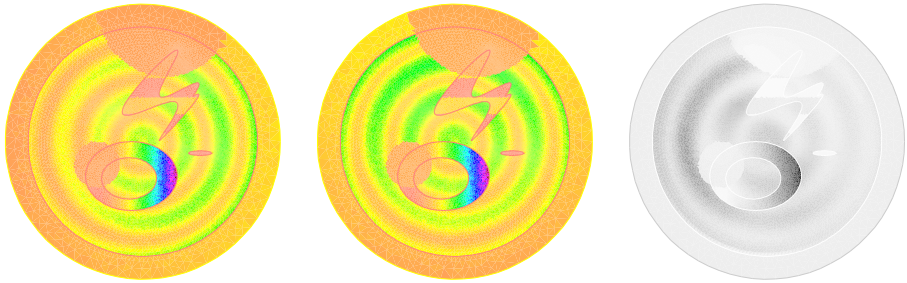

Figure 1.3: Perturbed reconstruction test. From left to right, the measured data for g_x and g_y, and the reconstructed conductivity after five iterations

Note that the pattern is recognizable from the data $\mathcal{E}$ itself. This may be expected: thanks to De Giorgi-Nash estimates, the potential u is continuous, thus the data displays the discontinuities of γ. However, the value of γ cannot be read from the data. The local character of the minimization procedure is striking. The solution does not seem to be affected by a substantial loss of data. If we limit the minimization procedure to the area outside the elliptical subdomains instead of considering false data, the optimal control procedure converges to a non-zero minimum, which is due to the background noise. The reconstructed pattern is very similar to the one presented in Figure 1.3.

1.4.2 Magneto-Acoustic Tomographies with Incomplete Data

Suppose that the measurements of $\partial p_z/\partial\nu(x,t)$ are only done on a part Γ of the boundary $\partial\Omega$. Suppose that T and Γ are such that they geometrically control Ω, which roughly means that every geometrical optic ray, starting at any point $x \in \Omega$, at time $t = 0$, hits Γ before time T at a nondiffractive point; see [10]. Let $\beta \in \mathcal{C}_0^\infty(\Omega)$ be a cutoff function such that $\beta(x) \equiv 1$ in a subdomain Ω' of Ω. Following [2], we construct by the geometrical control method a function $\widetilde{v}(x,t)$ satisfying (1.25), the initial condition $\widetilde{v}(x,0) = \beta(x)v_y(x,0)$ (v_y given by (1.28)), the boundary condition $\widetilde{v} = 0$ on $\partial\Omega\backslash\overline{\Gamma}$, and the final conditions (1.26). The reconstruction formulae (1.38) and (1.39) should be replaced by

$$c\gamma(z) \approx -\frac{2c_s|z-y|^2}{r^2}\int_0^T\int_\Gamma \frac{\partial p_z}{\partial\nu}(x,t)\widetilde{v}(x,t)\,d\sigma(x)\,dt, \tag{1.40}$$

and

$$\int_0^T\int_\Gamma \frac{\partial p_z}{\partial\nu}(x,t)\widetilde{v}(x,t)\,d\sigma(x)\,dt = c\frac{(y-z)\cdot\mathbf{e}}{4\pi|z-y|^3}. \tag{1.41}$$

1.5 Concluding Remarks

In this chapter, we have proposed two algorithms for solving the inverse problem in vibration potential tomography. Both algorithms are based on transforming the conductivity

equation into a nonlinear PDE. The first one follows from a perturbative approach while the second one follows an optimal control approach and can be applied to the case of incomplete data. It should be emphasized that from (1.4), an alternative way for solving the VPT problem is to first obtain $j = \gamma|\nabla v|$ in each D and then to replace γ by $j/|\nabla v|$ in the conductivity equation (1.1). This yields to exactly the same nonlinear problem as the one extensively investigated by Seo's group for Magnetic Resonance Electrical Impedance Tomography (MREIT). An efficient algorithm for solving the inverse problem in MREIT is the so-called $J-$substitution algorithm. See for instance [22, 23]. We believe that if we restrict the resolution in the $J-$substitution algorithm to the size of D, it would lead to the same quality of conductivity images as the one provided in this chapter. However, the algorithms developed here for VPT are simpler and use only one current.

For magneto-acoustic tomography with magnetic induction, we provided explicit inversion formulae. Magneto-acoustic tomography transforms the inverse conductivity problem into a much simpler inverse source problem. Because of the acoustic boundary conditions, the spherical Radon inverse transform can not be applied. Our approach is to make an appropriate averaging of the measurements by using particular solutions to the wave equation. Our approach extends easily to the case where only a part of the boundary is accessible.

It is worth noticing that our approach for the magneto-acoustic tomography can be used in photo-acoustic imaging (see [41] for a review of the current state-of-the-art of photo-acoustic imaging). We also intend to generalize our inversion formula to the case where the medium is acoustically inhomogeneous (contains small acoustical scatterers).

Chapter 2

Asymptotic Formulas for Thermography Based Recovery of Anomalies

2.1 Introduction

Medical thermal imaging has become a procedure of choice in the screening for breast, skin, or liver cancer [26]. It has the ability to identify various stages of disease development, and can pick up early stages which usually elude traditional anatomical examinations. Thermal imaging relies on the fact that chemical and blood vessel activity in pre-cancerous tissue and its surroundings are higher than in healthy tissue. Pre-cancerous and cancerous areas are characterized by heightened metabolism and require an abundant stream of nutrients to maintain growth. These extra nutrients are transported through various channels such as increased chemical activity, enhanced blood stream, and creation of new blood vessels (neoangiogenesis) [42]. This process results in a local increase in temperature.
Detection of these small temperature variations is made possible by state of the art imaging techniques. They involve ultra-sensitive thermal cameras and sophisticated software in detecting, analyzing, and producing high-resolution thermal images of vascular changes. More precisely, medical thermal imaging technique proceeds as follows: an infrared scanning device is used to convert infrared radiation emitted from the skin surface to electrical impulses. Those are then plotted on a color monitor. This map of body surface temperature is referred to as a thermogram. The spectrum of colors corresponds to a scale of infrared radiation emitted from the body surface. Since temperature distribution is highly isotropic in healthy tissue, subtle temperature anisotropies produce a clear imprint. See [1, 34].

Thermal imaging is a very reliable technology. In fact, clinical studies have shown that thermal imaging has an average sensitivity and specificity of 90% when applied to screening of breast tissue. As of today, an abnormal infrared image is the single most important

marker of high risk of onset breast cancer onset. Thermal imaging may also be used for different purposes such as

(i) assessing the extent of a previously diagnosed lesion;

(ii) localizing an abnormal area not previously identified, so further diagnostic tests can be performed;

(iii) detecting early lesions before they are clinically apparent;

(iv) guiding thermal ablation therapies.

In this chapter, we perform a quantitative study of temperature perturbation due to small thermal anomalies and we design algorithms for localizing these anomalies and estimating their size. We start from a realistic model in half space with convective boundary condition on the surface. It is noteworthy that our results can be applied to other types of thermography problems, such as the detection of buried objects in the underground. We seek to reconstruct only some rough feature of present anomalies. This partial reconstruction has the advantage to be stable against measurement noise and perturbation in geometry. Based on rigorously derived asymptotic estimates, we find an approximation formula that leads us to noniterative detection algorithms for finding dominant features of present anomalies.
We also consider in this chapter how to lay the mathematical background for ultrasonic temperature imaging. Ultrasonic temperature imaging is an essential tool for guiding medical devices in the course of thermal ablation therapy. It relies on the fact that sound speed in tissues depends on temperature. Thermal ablation therapy, such as focused ultrasound surgery, is a new way of destroying malignant tumors without damaging surrounding tissue. This technique consists of running the focused ultrasound surgery system at an initial, pre-ablative low intensity while using a diagnostic ultrasound imaging system to detect the associated localized temperature rise. This assumes that the temperature dependence of sound speed is known.

Let us now recall some previous results on anomaly detection by thermal imaging. In a recent paper [6], efficient noniterative algorithms for locating thermal anomalies from boundary measurements of temperature were introduced. The proposed reconstruction was based on a small volume assumption for the anomalies. The authors also assumed that the anomalies lay inside a bounded homogeneous domain, on whose boundary a heat flux was imposed. Resulting temperature was then measured on the same boundary. In another piece of work, Miller et al. [32] studied ultrasonic temperature imaging. Remarkably, their investigation lacks any mathematical analysis. We believe that a rigorous mathematical theory for the effects of thermal anomalies had to be investigated, since we want to perform a meticulate quantitative analysis. Ultimately this study should result in improving accuracy of lesion detection. In the following sections we will first present our novel mathematical analysis, we will then derive reconstruction algorithms. Numerical evidence validating these algorithms is presented in the last section of this chapter.

2.2 Physical Background, Non-dimensionalisation, Green's Function

2.2.1 Problem Statement

We consider the transient heat equation in the half space

$$\Omega = \{(x_1, x_2, x_3) \in \mathbb{R}^3 : x_3 < 0\} \tag{2.1}$$

in a homogeneous background of thermal conductivity k_0. The background contains regions (of small) volume where the conductivity is different. Denote D the union of all regions where the heat conductivity is different from k_0, and k the over all thermal conductivity function. We define $D = \cup_{j=1}^{m} D_j$, where the D_j's are such that $k(x)$ is equal to the positive constant k_j on D_j. If we denote τ the temperature function, τ satisfies [29]

$$\frac{\partial \tau}{\partial t} - \nabla \cdot (k \nabla \tau) = 0 \qquad \text{in } (\Omega \setminus \partial \overline{D}) \times (0, T), \tag{2.2}$$

$$k_0 (\nabla \tau \cdot \nu)^+ = k_j (\nabla \tau \cdot \nu)^- \qquad \text{on } \partial D_j \times (0, T), \tag{2.3}$$

$$\lim \tau(x, t) = \tau_0 \qquad \text{as } |x| \to \infty, \tag{2.4}$$

$$\tau(x, 0) = \tau_{init}(x) \qquad \text{in } \Omega, \tag{2.5}$$

$$-k_0 \nabla \tau \cdot e_3 = C_{cool}(\tau - \tau_{ext}) \qquad \text{on } \partial\Omega \times (0, T), \tag{2.6}$$

where τ_0 is the (constant) temperature at infinity, τ_{init} is the initial temperature profile, and condition (2.6) expresses the radiational cooling on the boundary of Ω. C_{cool} is a positive constant that provides thermal resistance and $\tau_{ext}(x_1, x_2, t)$ is an imposed exterior temperature.

2.2.2 Non-dimensionalisation

To obtain simpler equations we set

$$u(x,t) = \tau\Big(\frac{k_0}{C_{cool}} x, \frac{k_0}{C_{cool}^2} t\Big) - \tau_0$$

to obtain the following equations for u:

$$\frac{\partial u}{\partial t} - \Delta u = 0 \qquad \text{in } (\Omega \setminus \overline{D}) \times (0, T), \tag{2.7}$$

$$\frac{\partial u}{\partial t} - \nabla \cdot \Big(\frac{k}{k_0} \nabla u\Big) = 0 \qquad \text{in } D \times (0, T), \tag{2.8}$$

$$(\nabla u \cdot \nu)^+ = \frac{k_j}{k_0} (\nabla u \cdot \nu)^- \qquad \text{on } \partial D_j \times (0, T), \tag{2.9}$$

$$\lim u(x, t) = 0 \qquad \text{as } |x| \to \infty, \tag{2.10}$$

$$u(x, 0) = \tau_{init}\Big(\frac{k_0}{C_{cool}} x\Big) - \tau_0 =: u_{init} \qquad \text{on } \Omega, \tag{2.11}$$

$$\frac{\partial u}{\partial x_3} + u = \tau_{ext}\Big(\frac{k_0}{C_{cool}} x, \frac{k_0}{C_{cool}^2} t\Big) - \tau_0 := u_{ext} \qquad \text{on } \partial\Omega \times (0, T). \tag{2.12}$$

2.2.3 Existence, Uniqueness and Continuous Dependence on Initial Data and Boundary Condition of the Solution to the Perturbed Problem

From general PDE theory, an existence, uniqueness and continuous dependence on initial data and boundary condition result can be stated for the system (2.7)-(2.12).

Theorem 2.2.1 *Assume $u_{init} \in L^2(\Omega)$, $u_{ext} \in L^2(0,T;L^2(\partial\Omega))$, $f \in L^2(0,T;L^2(\Omega))$. There is a unique weak solution to the following problem:*

$$\frac{\partial u}{\partial t} - \nabla \cdot \Big(\frac{k}{k_0}\nabla u\Big) = f \qquad \text{in } \Omega \times (0,T), \tag{2.13}$$

$$u(x,0) = u_{init} \qquad \text{in } \Omega, \tag{2.14}$$

$$\frac{\partial u}{\partial x_3} + u = u_{ext} \qquad \text{on } \partial\Omega \times (0,T). \tag{2.15}$$

This solution satisfies the estimates

$$\|u\|_{L^2(0,T;H^1(\Omega))} \leq C\big(\|u_{init}\|_{L^2(\Omega)} + \|u_{ext}\|_{L^2(0,T;L^2(\partial\Omega))} + \|f\|_{L^2(0,T;L^2(\Omega))}\big), \tag{2.16}$$

where C is a positive constant depending only on the two positive constants $m_1 := \min \frac{k}{k_0}$ and $m_2 := \max \frac{k}{k_0}$.

Proof. The bilinear functional

$$a(u,v) = \int_\Omega \frac{k}{k_0}\nabla u \nabla v + \int_{\partial\Omega} uv,$$

defined on $H^1(\Omega) \times H^1(\Omega)$ satisfies

$$|a(u,v)| \leq (1+m_2)\|u\|_{H^1(\Omega)}\|v\|_{H^1(\Omega)}, \tag{2.17}$$

$$|a(u,u)| \geq m_1\|u\|^2_{H^1(\Omega)} - m_1\|u\|^2_{L^2(\Omega)}. \tag{2.18}$$

Define the continuous linear functional L on $H^1(\Omega)$ by

$$L(v) = \int_\Omega f(x,t)v(x)dx + \int_{\partial\Omega} u_{ext}(x,t)v(x)dx,$$

for almost all t in $(0,T)$. It follows from [11], [30] that the initial value problem

$$a(u(t),v) + \frac{d}{dt}(u(t),v)_{L^2(\Omega)} = (L(t),v)_{H^1(\Omega)',H^1(\Omega)}, \tag{2.19}$$

$$u(0) = u_{init}, \tag{2.20}$$

has a unique solution in $L^2(0,T;H^1(\Omega))$ that depends continuously on L and u_{init}. □

Remark 2.2.2 *We make the following remark on regularity. It is well known that the solution to* (2.19)-(2.20) *is smooth in* $(\Omega \setminus \overline{D}) \times (0,T)$ *and in* $D \times (0,T)$ *provided that* f *be smooth. Due to [31], if* L *and* u_{init} *are more regular, say* f *is such that* $(\frac{d}{dt})^j f$ *is in* $L^2(0,T;H^s_{loc}(\overline{\Omega}))$ *for* $j = 0,\dots,p$, u_{ext} *is such that* $(\frac{d}{dt})^j u_{ext}$ *is in* $L^2(0,T;H^{s+\frac{1}{2}}_{loc}(\partial\Omega))$ *for* $j = 0,\dots,p+1$, *and* u_{init} *is in* $H^{s+2}_{loc}(\overline{\Omega})$, *then* u *is such that* $(\frac{d}{dt})^j u$ *is in* $L^2(0,T;H^{s+2}_{loc}(\overline{\Omega} \setminus \overline{D}))$ *for* $j = 0,\dots,p+1$ *provided the compatibility conditions:*

$$\Big(\frac{\partial}{\partial x_1}\Big)^{s_1}\Big(\frac{\partial}{\partial x_2}\Big)^{s_2}\Big(\frac{\partial u_{init}}{\partial x_3} + u_{init}\Big) = \lim_{t\to 0}\Big(\frac{\partial}{\partial x_1}\Big)^{s_1}\Big(\frac{\partial}{\partial x_2}\Big)^{s_2} u_{ext} \text{ on } \partial\Omega, 0 \le s_1 + s_2 \le s$$

are satisfied.

2.2.4 Green's Function and Solution to the Unperturbed Problem

Setting

$$g(x_1,\xi_1,t) = \frac{1}{2\sqrt{\pi t}}\Big(e^{-\frac{(x_1-\xi_1)^2}{4t}} + e^{-\frac{(x_1+\xi_1)^2}{4t}} - 2\int_0^\infty e^{-\frac{(x_1+\xi_1+\eta)^2}{4t}-\eta}d\eta\Big) \tag{2.21}$$

it is known that g satisfies (see Sommerfeld's long rod solution [37])

$$\begin{aligned} &\partial_t g = \partial^2_{x_1} g && \text{if } t>0, \xi \neq x \text{ and } \xi \neq -x,\\ &\partial_{x_1} g - g = 0 && \text{at } x_1 = 0, \text{ for } t>0, \end{aligned}$$

and g is a fundamental solution to the heat equation in the rod, in the sense that the function h defined by

$$h = \int_0^t \int_0^\infty f(\xi_1,s) g(x_1,\xi_1,t-s), d\xi_1 ds$$

is 0 at time 0, and satisfies $(\partial_t - \partial^2_{x_1})h = f$ in $(0,\infty)^2$ and $\partial_{x_1} h - h = 0$ at $x_1 = 0$, for $t>0$, if f is smooth.

Based on g we construct two Green's functions adapted to our problem

$$\begin{aligned} G_1(x_1,x_2,x_3,\xi_1,\xi_2,\xi_3,t) = \\ \frac{1}{(2\sqrt{\pi t})^3} e^{-\frac{(x_1-\xi_1)^2+(x_2-\xi_2)^2}{4t}}\Big(e^{-\frac{(x_3-\xi_3)^2}{4t}} + e^{-\frac{(x_3+\xi_3)^2}{4t}} - 2\int_0^\infty e^{-\frac{(-x_3-\xi_3+\eta)^2}{4t}-\eta}d\eta\Big), \end{aligned}$$

$$G_2(x_1,x_2,x_3,\xi_1,\xi_2,t) = G_1(x_1,x_2,x_3,\xi_1,\xi_2,0,t).$$

Note that the integral term in G_1 can be re-expressed as

$$-2\int_0^\infty e^{-\frac{(-x_3-\xi_3+\eta)^2}{4t}-\eta}d\eta = -2\sqrt{\pi t}e^{-x_3-\xi_3+t}\mathrm{erfc}\Big(\frac{2t-x_3-\xi_3}{2\sqrt{t}}\Big),$$

where erfc is the complementary error function. If we define

$$u_1(x_1,x_2,x_3,t) = \int_{-\infty}^0\int_{-\infty}^\infty\int_{-\infty}^\infty f_1(\xi_1,\xi_2,\xi_3)G_1(x_1,x_2,x_3,\xi_1,\xi_2,\xi_3,t)d\xi_1d\xi_2d\xi_3, \quad (2.22)$$

$$u_2(x_1,x_2,x_3,t) = \int_0^t\int_{-\infty}^\infty\int_{-\infty}^\infty f_2(\xi_1,\xi_2,s)G_2(x_1,x_2,x_3,\xi_1,\xi_2,t-s)d\xi_1d\xi_2ds. \quad (2.23)$$

Then u_1 satisfies

$$\partial_t u_1 - \Delta u_1 = 0 \qquad \text{in } \Omega\times(0,\infty), \quad (2.24)$$

$$\partial_{x_3}u_1 + u_1 = 0 \qquad \text{on } \partial\Omega\times(0,\infty), \quad (2.25)$$

$$u_1(x_1,x_2,x_3,0) = f_1(x_1,x_2,x_3), \quad (2.26)$$

and u_2 satisfies

$$\partial_t u_2 - \Delta u_2 = 0 \qquad \text{in } \Omega\times(0,\infty), \quad (2.27)$$

$$\partial_{x_3}u_2 + u_2 = f_2 \qquad \text{on } \partial\Omega\times(0,\infty), \quad (2.28)$$

$$u_2(x_1,x_2,x_3,0) = 0. \quad (2.29)$$

Consequently if the thermal conductivity k is constant throughout Ω (or equivalently the set D is empty) problem (2.7)-(2.12) can be solved by convolution. The solution, denoted u_0 in that case is given by

$$u_0(x_1,x_2,t) = \int_{-\infty}^0\int_{-\infty}^\infty\int_{-\infty}^\infty u_{init}(\xi_1,\xi_2,\xi_3)G_1(x_1,x_2,x_3,\xi_1,\xi_2,\xi_3,t)d\xi_1d\xi_2d\xi_3 + \int_0^t\int_{-\infty}^\infty\int_{-\infty}^\infty u_{ext}(\xi_1,\xi_2,s)G_2(x_1,x_2,x_3,\xi_1,\xi_2,t-s)d\xi_1d\xi_2ds.$$

Remark 2.2.3 *Equations* (2.24)-(2.26) *assume some regularity on* f_1. *For example* (2.24) *and* (2.25) *are satisfied if* f_1 *is in* $L^2(\Omega)$ *and for* (2.26) *to be satisfied at a fixed point* x *we may require*

$$\lim_{\epsilon\to 0}\int_{|y|\le\epsilon}|f_1(x+y)-f_1(x)|dy = 0$$

Obtaining equations (2.27)-(2.29) *from* (2.23) *is not standard: we provide a proof in Appendix. It can be done under the assumptions* f_2 *is in* $L^2(\mathbb{R}^2\times(0,\infty))$ *and*

$$\lim_{\epsilon\to 0}\int_{0\le s\le\epsilon}\int_{|y|\le\epsilon}|f_2(x+y,t-s)-f_2(x,t)|dyds = 0,$$

for (2.52) *to be satisfied at* (x,t).

2.3 The Perturbed Temperature Field

2.3.1 A Preliminary Result

We now give a continuous dependence result for a problem similar to (2.7)-(2.15) with Special jump conditions across ∂D. The following proposition holds.

Proposition 2.3.1 *Let $\widetilde{D}$ be a region made up of a finite collection of bounded connected smooth domains $\widetilde{D_j}$, strictly included in Ω. Let α be a positive constant less than 1. As previously k is assumed to be equal to the positive constant k_j in $\widetilde{D_j}$ and k_0 in $\Omega \setminus \widetilde{D}$. There is a unique v in $L^2(0,T;H^1(\Omega))$ satisfying the problem*

$$\frac{\partial v}{\partial t} - \Delta v = F \qquad \text{in } (\Omega \setminus \partial\overline{\widetilde{D}}) \times (0,T), \tag{2.30}$$

$$\frac{\partial v}{\partial t} - \nabla \cdot \Big(\frac{k}{k_0}\nabla v\Big) = F \qquad \text{in } \widetilde{D} \times (0,T), \tag{2.31}$$

$$(\nabla v \cdot \nu)^+ - \frac{k_j}{k_0}(\nabla v \cdot \nu)^- = f \qquad \text{on } \partial\widetilde{D_j} \times (0,T), \tag{2.32}$$

$$v(x,0) = v_{init} \qquad \text{in } \Omega, \tag{2.33}$$

$$\frac{\partial v}{\partial x_2} + \alpha v = v_{ext} \qquad \text{on } \partial\Omega \times (0,T), \tag{2.34}$$

where F is in $L^2(0,T;L^2(\Omega))$, f is in $L^2(0,T;L^2(\partial D))$, v_{init} is in $L^2(\Omega)$, v_{ext} is in $L^2(0,T;L^2(\partial\Omega))$. Indeed,

$$\|v\|_{L^2(0,T;H^1(\Omega))} \le C(\|v_{init}\|_{L^2(\Omega)} + \|v_{ext}\|_{L^2(0,T;L^2(\partial\Omega))} + \|F\|_{L^2(0,T;L^2(\Omega))} + \|f\|_{L^2(0,T;L^2(\partial\mathcal{D}))}), \tag{2.35}$$

where C depends on $\min \frac{k}{k_0}$, $\max \frac{k}{k_0}$ but is independent of $\alpha \le 1$ and of $\widetilde{D}$.

Proof. Choose the functional L to be

$$L(v) = \int_\Omega F(x,t)v(x)dx + \int_{\partial\Omega} u_{ext}(x,t)v(x)dx + \int_{\partial\widetilde{D}} f(x,t)v(x)dx,$$

for almost all t in $(0,T)$, and a to be

$$a(u,v) = \int_\Omega \frac{k}{k_0}\nabla u \nabla v + \alpha \int_{\partial\Omega} uv.$$

It is clear that the proposition is a simple extension of Theorem (2.2.1). □

2.3.2 Equations for the Perturbed Part of the Temperature Field

We now assume that $D_j = z_j + \epsilon B_j$, where the z_j's are fixed points and ϵ is a dilation parameter tending to 0. We denote u_ϵ the corresponding solution to (2.7)-(2.12). We also assume that u_{init} is in $L^2(\Omega)$ and that and u_{ext} is in $L^2(0,T;L^2(\partial\Omega))$. The difference $v_\epsilon = u_\epsilon - u_0$ satisfies the following equations

$$\frac{\partial v_\epsilon}{\partial t} - \Delta v_\epsilon = 0 \qquad \text{in } (\Omega \setminus \overline{D}) \times (0,T), \tag{2.36}$$

$$\frac{\partial v_\epsilon}{\partial t} - \nabla \cdot \Big(\frac{k}{k_0}\nabla v_\epsilon\Big) = (\frac{k}{k_0} - 1)\Delta u_0 \qquad \text{in } D \times (0,T), \tag{2.37}$$

$$(\nabla v_\epsilon \cdot \nu)^+ - \frac{k_j}{k_0}(\nabla v_\epsilon \cdot \nu)^- = (\frac{k}{k_0} - 1)\nabla u_0 \cdot \nu \qquad \text{on } \partial D_j \times (0,T), \tag{2.38}$$

$$\lim v_\epsilon(x,t) = 0 \qquad \text{as } |x| \to \infty, \tag{2.39}$$

$$v_\epsilon(x,0) = 0 \qquad \text{in } \Omega, \tag{2.40}$$

$$\frac{\partial v_\epsilon}{\partial x_3} + v_\epsilon = 0 \qquad \text{on } \partial\Omega \times (0,T). \tag{2.41}$$

As u_0 is smooth in a neighborhood of D in the time interval (η, T) for $0 < \eta < T$, equations (2.36)-(2.41) imply due to proposition 2.3.1 that $\|v_\epsilon\|_{L^2(0,T;H^1(\Omega))} \leq CT^{\frac{1}{2}}\epsilon$.

2.3.3 The Correction Term

As in [6], set

$$V = v_\epsilon + \epsilon \sum_{j=1}^{m}\sum_{i=1}^{3} \partial_{x_i} u_0(z_j,t)\psi_{j,i}\Big(\frac{x - z_j}{\epsilon}\Big),$$

where $\psi_{j,i}$ satisfies

$$\Delta\psi_{j,i} = 0 \qquad \text{in } \mathbb{R}^3 \setminus \overline{\partial B_j},$$

$$(\psi_{j,i})^+ = (\psi_{j,i})^- \qquad \text{on } \partial B_j,$$

$$(\partial_\nu \psi_{j,i})^+ - \frac{k}{k_0}(\partial_\nu \psi_{j,i})^- = \Big(1 - \frac{k}{k_0}\Big)\partial_\nu x_i \qquad \text{on } \partial B_j,$$

$$\lim \psi_{j,i}(x) = 0 \qquad \text{as } |x| \to \infty.$$

Lemma 2.3.2 *We have $\psi_{j,i}(x) = O\big(\frac{1}{|x|^2}\big)$, and $\nabla\psi_{j,i}(x) = O\big(\frac{1}{|x|^3}\big)$. In particular, $\psi_{j,i}$ is in $L^2(\mathbb{R}^3)$.*

Proof. It is well known that $\psi_{j,i}$ can be expressed as the single layer potential $\int_{\partial B_j} h(x,y)\mu(y)dy$ for some density μ and where $h(x,y) = \frac{1}{4\pi|x-y|}$. It can be shown that $\int_{\partial B_j} \mu(y)dy = 0$ from where it follows that $\psi_{j,i}(x) = O\big(\frac{1}{|x|^2}\big)$ and $\nabla\psi_{j,i}(x) = O\big(\frac{1}{|x|^3}\big)$. □

The following result holds.

Theorem 2.3.3 *There exists a positive constant C independent of T and ϵ such that $\|V\|_{L^2(0,T;H^1(\Omega))} \leq CT^{\frac{1}{2}}\epsilon^{\frac{5}{2}}$.*

Proof. For the sake of simpler notations we assume in this proof that $m = 1$.

We first perform a rescaling by setting $v(x,t) = V(\epsilon x, \epsilon^2 t)$. v satisfies (2.30)-(2.34) with $m = 1$ and

$$F(x,t) = \epsilon^3 \sum_{i=1}^{3} (\partial_{x_i}\partial_t u_0)(z_1, \epsilon^2 t)\psi_i\Big(x - \frac{z_1}{\epsilon}\Big) \quad \text{in } \Omega \setminus \Big(\frac{z_1}{\epsilon} + B_1\Big) \times \Big(0, \frac{T}{\epsilon^2}\Big),$$

$$F(x,t) = \epsilon^3 \sum_{i=1}^{3} (\partial_{x_i}\partial_t u_0)(z_1, \epsilon^2 t)\psi_i\Big(x - \frac{z_1}{\epsilon}\Big) + \epsilon^2\Big(\frac{k}{k_0} - 1\Big)(\Delta u_0)(\epsilon x, \epsilon^2 t) \quad \text{in } \Big(\frac{z_1}{\epsilon} + B_1\Big) \times \Big(0, \frac{T}{\epsilon^2}\Big),$$

$$f(x,t) = \epsilon\Big(\frac{k}{k_0} - 1\Big)(\partial_\nu u_0)(\epsilon x, \epsilon^2 t) + \epsilon \sum_{i=1}^{3} (\partial_{x_i} u_0)(z_1, \epsilon^2 t)\Big(1 - \frac{k}{k_0}\Big)\partial_\nu x_i \quad \text{on } \Big(\frac{z_1}{\epsilon} + \partial B_1\Big) \times \Big(0, \frac{T}{\epsilon^2}\Big),$$

$$v_{init} = \epsilon \sum_{i=1}^{3} \partial_i u_0(z_j, 0)\psi_i\Big(x - \frac{z_1}{\epsilon}\Big) \quad \text{in } \Omega,$$

$$v_{ext} = \epsilon \sum_{i=1}^{3} \partial_i u_0(z_j, 0)(\partial_{x_3}\psi_i)\Big(x - \frac{z_1}{\epsilon}\Big) + \epsilon^2 \sum_{i=1}^{3} \partial_i u_0(z_j, 0)\psi_i\Big(x - \frac{z_1}{\epsilon}\Big) \quad \text{on } \partial\Omega, \text{ with the choice } \alpha = \epsilon.$$

It is easily seen that

$$\|F(x,t)\|^2_{L^2(\Omega)} \leq C\epsilon^4 \tag{2.42}$$

thus

$$\|F(x,t)\|^2_{L^2(0,T/\epsilon^2;L^2(\Omega))} \leq CT\epsilon^2. \tag{2.43}$$

Next, we estimate f. We set $y = x - \frac{z_1}{\epsilon}$. That way for y on $(\partial B_1) \times \Big(0, \frac{T}{\epsilon^2}\Big)$

$$f(x,t) = f\Big(y + \frac{z_1}{\epsilon}, t\Big) = \epsilon\Big(\frac{k}{k_0} - 1\Big)(\partial_\nu u_0)(\epsilon y + z_1, \epsilon^2 t) + \epsilon \sum_{i=1}^{3} (\partial_{x_i} u_0)(z_1, \epsilon^2 t)\Big(1 - \frac{k}{k_0}\Big)\partial_\nu y_i,$$

and using the fact that u_0 is smooth in $\Omega \times (0,T)$, we see that f is bounded in the sup norm by $C\epsilon^2$, from which it follows that

$$\|f(x,t)\|^2_{L^2(\partial B_1)} \leq C\epsilon^4 \tag{2.44}$$

thus

$$\|f(x,t)\|^2_{L^2(0,T/\epsilon^2;L^2(\partial B_1)} \leq CT\epsilon^2. \tag{2.45}$$

It is also clear that

$$\|v_{init}\|^2_{L^2(\Omega)} \leq C\epsilon^2. \tag{2.46}$$

Finally, we estimate v_{ext}. Denote (z_{11}, z_{12}, z_{13}) the coordinates of z_1. For $x = (x_1, x_2, 0)$ on $\partial\Omega$

$$\left|x - \frac{z_1}{\epsilon}\right|^2 = \left(x_1 - \frac{z_{11}}{\epsilon}\right)^2 + \left(x_2 - \frac{z_{12}}{\epsilon}\right)^2 + \left(\frac{z_{13}}{\epsilon}\right)^2.$$

We find due to the decay of $(\partial_{x_3}\psi_{j,i})$ that

$$\left\|(\partial_{x_3}\psi_i)\Big(x - \frac{z_1}{\epsilon}\Big)\right\|^2_{L^2(\partial\Omega)} \leq C\int_0^\infty \frac{\rho d\rho}{\rho^6 + (\frac{z_{13}}{\epsilon})^6} \leq C\epsilon^4,$$

and due to the decay of $\psi_{j,i}$ that

$$\left\|\psi_i\Big(x - \frac{z_1}{\epsilon}\Big)\right\|^2_{L^2(\partial\Omega)} \leq C\int_0^\infty \frac{\rho d\rho}{\rho^4 + (\frac{z_{13}}{\epsilon})^4} \leq C\epsilon^2.$$

We infer,

$$\|v_{ext}\|^2_{L^2(\partial\Omega)} \leq C\epsilon^6 \tag{2.47}$$

thus

$$\|v_{ext}\|^2_{L^2(0,T/\epsilon^2;L^2(\partial\Omega))} \leq CT\epsilon^4. \tag{2.48}$$

We now apply (2.35) to obtain that

$$\|v(x,t)\|^2_{L^2(0,T/\epsilon^2;H^1(\Omega))} \leq CT\epsilon^2$$

and changing variables yields

$$\begin{aligned}
&\|V(x,t)\|^2_{L^2(0,T;L^2(\Omega))} \leq \epsilon^5\|v(x,t)\|^2_{L^2(0,T/\epsilon^2;L^2(\Omega))} \leq CT\epsilon^7,\\
&\|\nabla_x V(x,t)\|^2_{L^2(0,T;L^2(\Omega))} \leq \epsilon^3\|\nabla_x v(x,t)\|^2_{L^2(0,T/\epsilon^2;L^2(\Omega))} \leq CT\epsilon^5,
\end{aligned}$$

as desired. □

2.4 The Two-Dimensional Case

Section 2.2 can be adjusted to a two dimensional model by making a few straightforward modifications. We make these adjustments explicit only for the expression for the Green's function for the homogeneous problem. Adjusting section 2 is less obvious and will require the introduction of a cut off function.

2.4.1 Straightforward Modifications of Green's Function to Fit the 2D Case

Based on g defined in (2.21) we construct two Green's functions adapted to our problem

$$G_1(x_1,x_2,\xi_1,\xi_2,t)=\frac{1}{4\pi t}e^{-\frac{(x_1-\xi_1)^2}{4t}}\Big(e^{-\frac{(x_2-\xi_2)^2}{4t}}+e^{-\frac{(x_2+\xi_2)^2}{4t}}-2\int_0^\infty e^{-\frac{(-x_2-\xi_2+\eta)^2}{4t}-\eta}d\eta\Big),$$
$$G_2(x_1,x_2,\xi_1,t)=G_1(x_1,x_2,\xi_1,0,t).$$

If we define

$$u_1(x_1,x_2,t)=\int_{-\infty}^{\infty}\int_{-\infty}^{0}f_1(\xi_1,\xi_2)G_1(x_1,x_2,\xi_1,\xi_2,t)d\xi_2d\xi_1, \tag{2.49}$$
$$u_2(x_1,x_2,t)=\int_0^t\int_{-\infty}^{\infty}f_2(\xi_1,s)G_2(x_1,x_2,\xi_1,t-s)d\xi_1ds. \tag{2.50}$$

Then u_1 satisfies

$$\begin{aligned}&\partial_t u_1-\Delta u_1=0 && \text{in } \Omega\times(0,\infty),\\ &\partial_{x_2}u_1+u_1=0 && \text{on } \partial\Omega\times(0,\infty),\\ &u_1(x_1,x_2,0)=f_1(x_1,x_2), && \text{on } \partial\Omega\end{aligned}$$

and u_2 satisfies

$$\partial_t u_2-\Delta u_2=0 \quad \text{in } \Omega\times(0,\infty), \tag{2.51}$$
$$\partial_{x_2}u_2+u_2=f_2 \quad \text{on } \partial\Omega\times(0,\infty), \tag{2.52}$$
$$u_1(x_1,x_2,0)=0. \quad \text{on } \partial\Omega. \tag{2.53}$$

Consequently, if the thermal conductivity k is constant throughout Ω (or equivalently the set D is empty) problem (2.7)-(2.12) can be solved by convolution. The solution, denoted u_0 in that case is given by

$$u_0(x_1,x_2,t)=$$
$$\int_{-\infty}^{\infty}\int_{-\infty}^{0}u_{init}(\xi_1,\xi_2)G_1(x_1,x_2,\xi_1,\xi_2,t)d\xi_2d\xi_1+\int_0^t\int_{-\infty}^{\infty}u_{ext}(\xi_1,s)G_2(x_1,x_2,\xi_1,t-s)d\xi_1ds.$$

2.4.2 Special Corrector Obtained by Introducing a Cut off Function

The definition of the difference v_ϵ between the homogeneous and perturbed heat profiles is the same in the two dimensional case: equations (2.36)-(2.41) apply in that case too. Proposition 2.3.1 may be used as well in the two dimensional case. It is the insufficiently rapid decay of $\psi_{j,i}$ at infinity that makes the two dimensional case distinct, as explained further down.

Let $\psi_{j,i}$ satisfy

$$\begin{aligned}
&\Delta\psi_{j,i} = 0 && \text{in } \mathbb{R}^2 \setminus \partial\overline{B_j},\\
&(\psi_{j,i})^- = (\psi_{j,i})^+ && \text{on } \partial B_j,\\
&(\partial_\nu\psi_{j,i})^+ - \frac{k}{k_0}(\partial_\nu\psi_{j,i})^- = \Big(1 - \frac{k}{k_0}\Big)\partial_\nu x_i && \text{on } \partial B_j,\\
&\lim \psi_{j,i}(x) = 0 && \text{as } |x| \to \infty.
\end{aligned}$$

The following lemma holds.

Lemma 2.4.1 *We have $\psi_{j,i}(x) = O(\frac{1}{|x|})$, and $\nabla\psi_{j,i}(x) = O(\frac{1}{|x|^2})$. Moreover, $\psi_{j,i}$ is not in general in $L^2(\mathbb{R}^2)$.*

Proof. In the two dimensional case too $\psi_{j,i}$ can be expressed as the single layer potential $\int_{\partial B_j} h(x,y)\mu(y)dy$ for some density μ and where this time $h(x,y) = -\frac{1}{2\pi}\log|x-y|$. It can be shown that $\int_{\partial B_j}\mu(y)dy = 0$ from where it follows that $\psi_{j,i}(x) = O\big(\frac{1}{|x|}\big)$ and $\nabla\psi_{j,i}(x) = O\big(\frac{1}{|x|^2}\big)$. □

Finally as a closed form expression for $\psi_{j,i}$ in the case where B_j is the unit disk centered at the origin is given by

$$\psi_{j,i}(x) = \begin{cases} \frac{k_0-k}{k_0+k}x_i & \text{in } B_j,\\ \frac{k_0-k}{k_0+k}\frac{x_i}{|x|^2} & \text{in } \mathbb{R}^2 \setminus \overline{B_j}, \end{cases}$$

we conclude that $\psi_{j,i}(x)$ is not in $L^2(\mathbb{R}^2)$ in that case.

Fix a function ρ in $\mathcal{C}^\infty(\mathbb{R}^2)$ such that

$$\rho(x) = \begin{cases} 1 & \text{if } |x| \le 1,\\ 0 & \text{if } |x| \ge 2. \end{cases}$$

Set

$$V = v_\epsilon + \epsilon\sum_{j=1}^{m}\sum_{i=1}^{2}\partial_{x_i}u_0(z_j,t)\psi_{j,i}\Big(\frac{x-z_j}{\epsilon}\Big)\rho(\epsilon x). \tag{2.54}$$

Notice that

$$\Big\|\psi_{j,i}\Big(\frac{x-z_j}{\epsilon}\Big)\rho(\epsilon x)\Big\|^2_{L^2(\Omega)} \le C\epsilon^2|\log\epsilon|.$$

2.4.3 Derivation of the Order of the Estimate

Our main result is the following theorem.

Theorem 2.4.2 *There exists a positive constant C independent of T and ϵ such that $\|V\|_{L^2(0,T;H^1(\Omega))} \leq CT^{\frac{1}{2}}\epsilon^2|\log\epsilon|^{\frac{1}{2}}$, for the two-dimensional case.*

Proof. For the sake of simpler notations we assume that $m = 1$.

First we rescale $v(x,t) = V(\epsilon x, \epsilon^2 t)$. v satisfies (2.30)-(2.34) with $m = 1$ and

$$F(x,t) = \epsilon^3 \sum_{i=1}^{2} (\partial_{x_i}\partial_t u_0)(z_j,\epsilon^2 t) psi_i\Big(x - \frac{z_1}{\epsilon}\Big)\rho(\epsilon^2 x) + (\partial_{x_i} u_0)(z_j,\epsilon^2 t)\Big[\nabla\psi_i\Big(x-\frac{z_1}{\epsilon}\Big)\nabla\rho(\epsilon^2 x) + \epsilon\psi_i\Big(x-\frac{z_1}{\epsilon}\Big)\Delta\rho(\epsilon^2 x)\Big]$$

$$\text{in } \Omega \setminus \Big(\frac{z_1}{\epsilon} + B_1\Big) \times \Big(0, \frac{T}{\epsilon^2}\Big),$$

$$F(x,t) = \epsilon^3 \sum_{i=1}^{2} (\partial_{x_i}\partial_t u_0)(z_1,\epsilon^2 t)\psi_i\Big(x - \frac{z_1}{\epsilon}\Big) + \epsilon^2\Big(\frac{k}{k_0} - 1\Big)(\Delta u_0)(\epsilon x, \epsilon^2 t)$$

$$, \qquad \text{in } \Big(\frac{z_1}{\epsilon} + B_1\Big) \times \Big(0, \frac{T}{\epsilon^2}\Big)$$

$$f(x,t) = \epsilon\Big(\frac{k}{k_0} - 1\Big)(\partial_\nu u_0)(\epsilon x, \epsilon^2 t) + \epsilon \sum_{i=1}^{2} (\partial_{x_i} u_0)(z_j,\epsilon^2 t)\Big(1 - \frac{k}{k_0}\Big)\partial_\nu x_i$$

$$, \qquad \text{on } \Big(\frac{z_1}{\epsilon} + \partial B_1\Big) \times \Big(0, \frac{T}{\epsilon^2}\Big)$$

$$v_{init} = \epsilon \sum_{i=1}^{2} \partial_i u_0(z_j, 0)\psi_i\Big(x - \frac{z_1}{\epsilon}\Big)\rho(\epsilon^2 x),$$

$$\text{in } \Omega,$$

$$v_{ext} = \epsilon \sum_{i=1}^{2} \partial_i u_0(z_j,0)(\partial_{x_2}\psi_i)\Big(x - \frac{z_1}{\epsilon}\Big)\rho(\epsilon^2 x) + \epsilon\partial_i u_0(z_j,0)\psi_i\Big(x-\frac{z_1}{\epsilon}\Big)(\partial_{x_2}\rho)(\epsilon^2 x) + \epsilon^2 \sum_{i=1}^{2} \partial_i u_0(z_j,0)\psi_i\Big(x-\frac{z_1}{\epsilon}\Big)\rho(\epsilon^2 x)$$

$$\text{on } \partial\Omega \text{ with the choice } \alpha = \epsilon.$$

It is easily seen that

$$\|F(x,t)\|^2_{L^2(\Omega)} \leq C\epsilon^4 \tag{2.55}$$

thus

$$\|F(x,t)\|^2_{L^2(0,T/\epsilon^2;L^2(\Omega))} \leq CT\epsilon^2. \tag{2.56}$$

Next, using the fact that u_0 is smooth in $\Omega \times (0,T)$, we obtain just as in the three dimensional case

$$\|f(x,t)\|^2_{L^2(\partial B_1)} \leq C\epsilon^4 \tag{2.57}$$

thus

$$\|f(x,t)\|^2_{L^2(0,T/\epsilon^2;L^2(\partial B_1))} \leq CT\epsilon^2. \tag{2.58}$$

It is also clear that

$$\|v_{init}\|^2_{L^2(\Omega)} \leq C\epsilon^2|\log\epsilon|. \tag{2.59}$$

Finally we estimate v_{ext}. Denote (z_{11}, z_{12}) the coordinates of z_1. For $x = (x_1, 0)$ on $\partial\Omega$

$$\Big|x - \frac{z_1}{\epsilon}\Big|^2 = \Big(x_1 - \frac{z_{11}}{\epsilon}\Big)^2 + \Big(\frac{z_{12}}{\epsilon}\Big)^2.$$

We find due to the decay of $(\partial_{x_2}\psi_{j,i})$ that

$$\Big\|(\partial_{x_2}\psi_i)\Big(x - \frac{z_1}{\epsilon}\Big)\rho(\epsilon^2 x)\Big\|^2_{L^2(\partial\Omega)} \leq C\int_0^\infty \frac{d\rho}{\rho^4 + (\frac{z_{13}}{\epsilon})^4} \leq C\epsilon^3,$$

and due to the decay of $\psi_{j,i}$ that

$$\Big\|\psi_i\Big(x - \frac{z_1}{\epsilon}\Big)\partial_{x_2}\rho(\epsilon^2 x)\Big\|^2_{L^2(\partial\Omega)} \leq C\int_0^\infty \frac{d\rho}{\rho^2 + (\frac{z_{13}}{\epsilon})^2} \leq C\epsilon,$$
$$\Big\|\psi_i\Big(x - \frac{z_1}{\epsilon}\Big)\rho(\epsilon^2 x)\Big\|^2_{L^2(\partial\Omega)} \leq C\int_0^\infty \frac{d\rho}{\rho^2 + (\frac{z_{13}}{\epsilon})^2} \leq C\epsilon.$$

We infer,

$$\|v_{ext}\|^2_{L^2(\partial\Omega)} \leq C\epsilon^5 \tag{2.60}$$

thus

$$\|v_{ext}\|^2_{L^2(0,T/\epsilon^2;L^2(\partial\Omega))} \leq CT\epsilon^3. \tag{2.61}$$

We now apply (2.35) to obtain that

$$\|v(x,t)\|^2_{L^2(0,T/\epsilon^2;H^1(\Omega))} \leq CT\epsilon^2|\log\epsilon|,$$

and changing variables yields

$$\|V(x,t)\|^2_{L^2(0,T;L^2(\Omega))} \leq \epsilon^4\|v(x,t)\|^2_{L^2(0,T/\epsilon^2;L^2(\Omega))} \leq CT\epsilon^6|\log\epsilon|,$$
$$\|\nabla_x V(x,t)\|^2_{L^2(0,T;L^2(\Omega))} \leq \epsilon^2\|\nabla_x v(x,t)\|^2_{L^2(0,T/\epsilon^2;L^2(\Omega))} \leq CT\epsilon^4|\log\epsilon|,$$

as desired. □

2.5 The Resulting Expansion After Multiplication by a Test Function and Integration on the Surface Plane

Suppose that the space dimension is 3. Let ϕ be in $L^2(0,T;H^1(\Omega))$ such that

$$(\partial_t + \Delta)\phi = 0 \qquad \text{in } \Omega \times (0,T), \tag{2.62}$$

$$\phi(.,T) = 0 \qquad \text{in } \Omega. \tag{2.63}$$

Let v_ϵ satisfy (2.36)-(2.41). We find by integration by parts and application of Theorem 2.3.3,

$$\int_0^T \int_{\partial\Omega} v_\epsilon(\frac{\partial\phi}{\partial x_3} + \phi) = \epsilon^3 \sum_{j=1}^m (\frac{k_j}{k_0} - 1) \int_0^T \sum_{i=1}^3 \partial_{x_i} u_0(z_j,t) \int_{B_j} \nabla\psi_{j,i}(x)\nabla\phi(z_j,t) \tag{2.64}$$

$$+R, \tag{2.65}$$

where the remainder R is bounded on $D \times (0,T)$ by $CT\epsilon^4 \sup|\nabla\phi|$.

A calculation shows that $\{\int_{B_j} \nabla\psi_{j,i}(x)\}_{i=1,2,3}$ can be replaced by the polarization tensor $M^{(j)}$ (depending only on B_j and k_j/k_0) to obtain

$$\int_0^T \int_{\partial\Omega} v_\epsilon\Big(\frac{\partial\phi}{\partial x_3} + \phi\Big) = \epsilon^3 \sum_{j=1}^m \Big(\frac{k_j}{k_0} - 1\Big) \int_0^T \nabla u_0(z_j,t) M^{(j)} \nabla\phi(z_j,t) \tag{2.66}$$

$$+R. \tag{2.67}$$

In the two-dimensional case, the cut off section appearing in formula (2.54) goes away by integration on a bounded set. We obtain,

$$\int_0^T \int_{\partial\Omega} v_\epsilon\Big(\frac{\partial\phi}{\partial x_2} + \phi\Big) = \epsilon^2 \sum_{j=1}^m \Big(\frac{k_j}{k_0} - 1\Big) \int_0^T \nabla u_0(z_j,t) M^{(j)} \nabla\phi(z_j,t) \tag{2.68}$$

$$+R, \tag{2.69}$$

for ϕ satisfying (2.62),(2.63), and where R is bounded on $D\times(0,T)$ by $CT\epsilon^3|\log\epsilon|^{\frac{1}{2}} \sup|\nabla\phi|$.

We summarize in the following theorem our main results in this chapter.

Theorem 2.5.1 **(i)** *The following asymptotic expansions of the weighted boundary measurements hold:*

$$\begin{aligned}\int_0^T \int_{\partial\Omega} (u_\epsilon - u_0)\Big(\frac{\partial\phi}{\partial x_d} + \phi\Big) &= \epsilon^d \sum_{j=1}^m \Big(\frac{k_j}{k_0} - 1\Big) \int_0^T \nabla u_0(z_j,t) M^{(j)} \nabla\phi(z_j,t) \\ &+ \begin{cases} O(T\epsilon^4 \sup_{D\times(0,T)} |\nabla\phi|) & \text{for } d = 3, \\ O(T\epsilon^3|\log\epsilon|^{\frac{1}{2}} \sup_{D\times(0,T)} |\nabla\phi|) & \text{for } d = 2. \end{cases}\end{aligned}$$

(ii) *The following inner expansions hold. We have in the two-dimensional case*

$$\Big\|u_\epsilon - u_0 + \epsilon \sum_{j=1}^{m}\sum_{i=1}^{2} \partial_{x_i} u_0(z_j,t)\psi_{j,i}\Big(\frac{x-z_j}{\epsilon}\Big)\rho(\epsilon x)\Big\|_{L^2(0,T;H^1(\Omega))} \leq CT^{\frac{1}{2}}\epsilon^2|\log\epsilon|^{\frac{1}{2}},$$

where $\rho \in \mathcal{C}^\infty(\mathbb{R}^2)$ *is such that* $\rho(x) = 1$ *if* $|x| \leq 1, \rho(x) = 0$ *if* $|x| \geq 2$, *while in three dimensions*

$$\Big\|u_\epsilon - u_0 + \epsilon \sum_{j=1}^{m}\sum_{i=1}^{3} \partial_{x_i} u_0(z_j,t)\psi_{j,i}\Big(\frac{x-z_j}{\epsilon}\Big)\Big\|_{L^2(0,T;H^1(\Omega))} \leq CT^{\frac{1}{2}}\epsilon^{\frac{5}{2}}.$$

The weighted boundary measurements will be used in the next section to design non-iterative algorithms for detecting the anomalies from boundary measurements while the inner expansions form the basis of the reconstruction method from ultrasonic thermal measurements. The inner expansions allow to reconstruct the anomalies with much better spatial and contrast resolutions than the weighted measurements which only. In fact, the inner expansions uniquely characterize the shape and the thermal conductivity of the anomaly. In contrast, the asymptotic expansions of the weighted measurements show that, from an imaging point of view, the location and the polarization tensor of the anomaly are the only quantities that can be determined from boundary measurements.

2.6 Examples of Applications

2.6.1 Active Temperature Imaging

Suppose for the sake of simplicity that $d = 2$ and all the anomalies are disks. Choose $u_{ext} = \delta_{t=0}\delta_y$ for some point $y \in \partial\Omega$ and $u_{init} = 0$ in Ω. The unperturbed solution corresponds to $u_0(x,t) = G_2(x,y,t)$. Choose $\phi(x,t) = G_2(x,y',T-t)$, where $y' \in \partial\Omega$. The asymptotic formula for the weighted boundary measurements yields

$$(u_\epsilon - u_0)(y',T) \approx 2\epsilon^2 \sum_{j=1}^{m} \Big(\frac{k_j}{k_0} - 1\Big)\frac{|B_j|}{1+\frac{k_j}{k_0}} \int_0^T \nabla G_2(z_j,y,t)\cdot\nabla G_2(z_j,y',T-t)dt.$$

Let now $y, y' \in \{y_1,\ldots,y_n\}$, where $y_1,\ldots,y_n$ are source points on $\partial\Omega$. Define the matrix $A = \{A_{ll'}\}_{l,l'=1}^n$ by

$$A_{ll'} := 2\epsilon^2 \sum_{j=1}^{m} \Big(\frac{k_j}{k_0} - 1\Big)\frac{|B_j|}{1+\frac{k_j}{k_0}} \int_0^T \nabla G_2(z_j,y_l,t)\cdot\nabla G_2(z_j,y_{l'},T-t)dt.$$

For $z \in \Omega$, we decompose the symmetric real matrix C defined by

$$C := \Big[\int_0^T \nabla G_2(z,y_l,t)\cdot\nabla G_2(z,y_{l'},T-t)dt\Big]_{l,l'=1,\ldots,n}$$

as follows

$$C = \sum_{l=1}^{p} v_l(z) v_l^*(z)$$

for some $p \leq n$, where v_l^* denotes the transpose of v_l. By exactly the same arguments as those in [6], the following characterization of the range of the matrix A holds:

$$v_l(z) \in \text{Range}(A) \; \forall l \in \{1, \ldots, p\} \text{ iff } z \in \{z_1, \ldots, z_m\}.$$

Let the singular value decomposition (SVD) of the matrix A be defined by $A = U\Sigma V^*$. Let U_{signal} denote the first columns of U that provide a basis for the column space of A and U_{noise} the rest of the matrix U which provides a basis for the left null space of A. From the characterization of the range of A, a test point z coincides with one of the locations z_j if and only if $P(v_l(z)) = 0$, where $P = I - U_{signal} U_{signal}^*$ is the orthogonal projection onto the null space of A. Thus we can form an image of the locations $\{z_j\}_{j=1}^m$ by plotting, at each z in a box search, the quantities

$$W_l(z) := \frac{1}{||P(v_l(z))||} \quad \text{for } l = 1, \ldots, p.$$

The resulting plot will have large peaks at the locations of $z_j, j = 1, \ldots, m$.

The matrix A is known from measurements of $(u_\epsilon - u_0)(y', T)$, where $u_0(x,t) = G_2(x,y,t)$ and $y, y' \in \{y_1, \ldots, y_n\}$.

Other choices for heating are possible. For example, we can place the heat source in the upper half space by choosing

$$u_{ext}(x,t) = \frac{1}{t}\left[\exp\Big(- \frac{|x-y|^2}{4t} \Big) + \frac{\partial}{\partial x_2} \exp\Big(- \frac{|x-y|^2}{4t} \Big) \right] \quad \text{for } x \in \partial\Omega,$$

and $y \in \mathbb{R}^2 \setminus \Omega$. Then we take

$$\phi(x,t) = \frac{1}{(T-t)} \exp\Big(- \frac{|x-y|^2}{4(T-t)} \Big),$$

for $y' \in \mathbb{R}^2 \setminus \Omega$ and $u_{init} = 0$ in Ω. Set $y, y' \in \{y_1, \ldots, y_n\}$, where $y_l \in \mathbb{R}^2 \setminus \overline{\Omega}$. Construct the matrix A from the weighted measurements $\int_0^T \int_{\partial\Omega} (u_\epsilon - u_0)\big(\frac{\partial \phi}{\partial x_d} + \phi\big)$. The same imaging algorithm applies when $v_l(z)$ is constructed from the decomposition of the matrix

$$\left[\int_0^T \nabla G(z, y_l, t) \cdot \nabla G(z, y_{l'}, T-t) dt \right]_{l,l'=1,\ldots,n},$$

where $G(z,y,t) = \frac{1}{t} \exp\big(- \frac{|z-y|^2}{4t} \big)$.

Because of the singularity of G_2 on the boundary $\partial\Omega$, the second choice of heating is easier to implement numerically.

In the following example, two anomalies of radius 0.3 and 0.1 and conductivities 2 and 5 are placed at $(-2, -1.5)$ and $(2.5, -2.5)$, respectively. We set $T = 1$ and the conductivity of the background equals to 0.1. We choose $n = 10$ heat sources placed at the same $x_2 > 0$ and at $x_1^l = -5 + 10\frac{l-1}{9}, l = 1, \ldots 10$. Figures 2.1 and 2.2 show the reconstructions without and with noise.

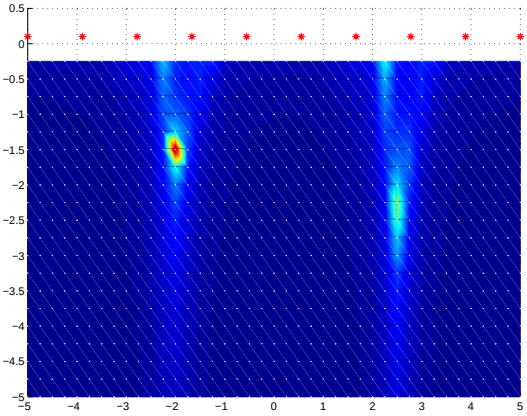

Figure 2.1: Detection of anomalies

In Figure 2.1, we see clearly the presence of two anomalies. However, the one on the right is less clearer than the one on the left because it is deeper.

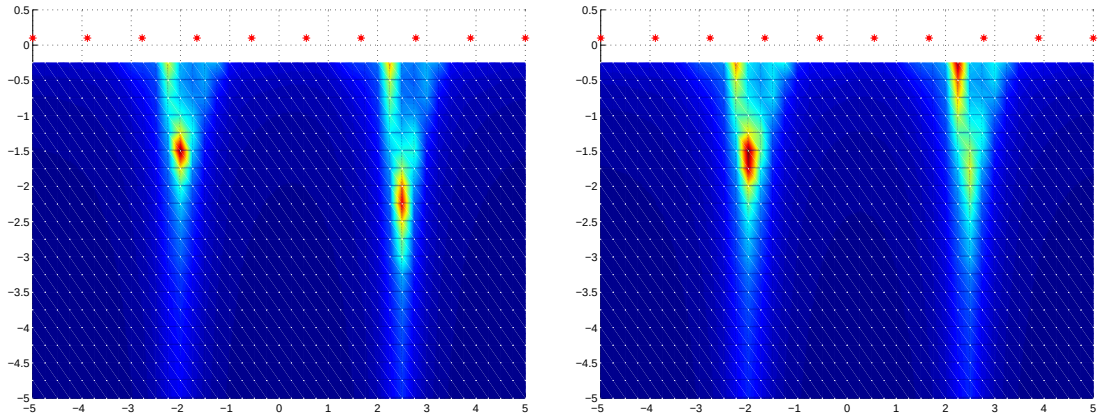

Figure 2.2: Detection in the presence of 1% (on the left) and 5% (on the right) of noise.

2.6.2 Passive Temperature Imaging

This appears to be a harder problem as no forcing can be imposed. The process is passive and driven by cooling. Choose u_{init} in the form $e^{\alpha x_3}$, $\alpha > 0$ and u_{ext} linear in time to simulate cooling: $u_{ext}(x, t) = 1 + \alpha - \beta t$, for $x \in \partial\Omega$.

The unperturbed solution $u_0(x,t)$ has the following form:

$$u_0(x_1,\ldots,x_d,t) = \int_{-\infty}^{0} \widetilde{u}_{init}(\xi_d)\widetilde{G}_1(x_d,\xi_d,t)d\xi_d + \int_0^t \widetilde{u}_{ext}(s)\widetilde{G}_2(x_d,t-s)ds, \tag{2.70}$$

where $\widetilde{G}_1(x_d,\xi_d,t)$ is given by

$$\widetilde{G}_1(x_d,\xi_d,t) = \frac{1}{\sqrt{4\pi t}}\Big(e^{-\frac{(x_d-\xi_d)^2}{4t}} + e^{-\frac{(x_d+\xi_d)^2}{4t}} - 2\int_0^{+\infty} e^{-\frac{(x_d+\xi_d-\eta)^2}{4t}-\eta}d\eta\Big), \tag{2.71}$$

and $\widetilde{G}_2(x_d,t) = \widetilde{G}_1(x_d,0,t)$.

It is easy to see that the gradient of unperturbed solution u_0 has only one nontrivial component:

$$\nabla_x u_0(x,t) = \begin{pmatrix} 0 \\ \vdots \\ \int_{-\infty}^{0} \widetilde{u}_{init}(\xi_d)\frac{\partial\widetilde{G}_1}{\partial x_d}(x_d,\xi_d,t)d\xi_d + \int_0^t \widetilde{u}_{ext}(s)\frac{\partial\widetilde{G}_2}{\partial x_d}(x_d,t-s)ds \end{pmatrix}. \tag{2.72}$$

Suppose for the sake of simplicity that $d=2$ and all the anomalies are disks.

For $y=(y_1,y_2)$ in the upper half-space, choose

$$\phi(x,t) = \phi(x,y,t,T) := \frac{1}{(T-t)}\exp\Big(-\frac{|x-y|}{4(T-t)}\Big),$$

as in the above section. For $j=1,\ldots,m$, write $z_j = (z_j^{(1)}, z_j^{(2)})$. It is easy to see from Theorem 2.5.1 that for fixed y_2 the functional

$$I_\phi(T) := \int_0^T \int_{\partial\Omega} (u_\epsilon - u_0)\Big(\frac{\partial\phi}{\partial x_d} + \phi\Big)$$

has extrema for $y_1 = z_j^{(1)}, j=1,\ldots,m$.

To verify the validity the asymptotic expansion in Theorem 2.5.1, we compare the values of $I_\phi(T)$ as a function of y_1 computed directly with those given by the asymptotic formula. Here $y_2 = 0.1$ and $T = 0.1$. Figure 2.3 shows these comparisons for an inclusion located at $(-2,-1.5)$ with different radius $(0.005, 0.01, 0.1$ and $0.2)$ and different thermal conductivities $1.5, 2, 3$ and 4. The approximation error gets larger with the radius of the anomaly.

As we can see from Figure 2.3, the first order of magnitude given by the asymptotic expansion formula is valid for the anomalies of radius 0.005 and 0.01. On the contrary, for the anomalies of radius 0.1 and 0.2 there is a significant error.

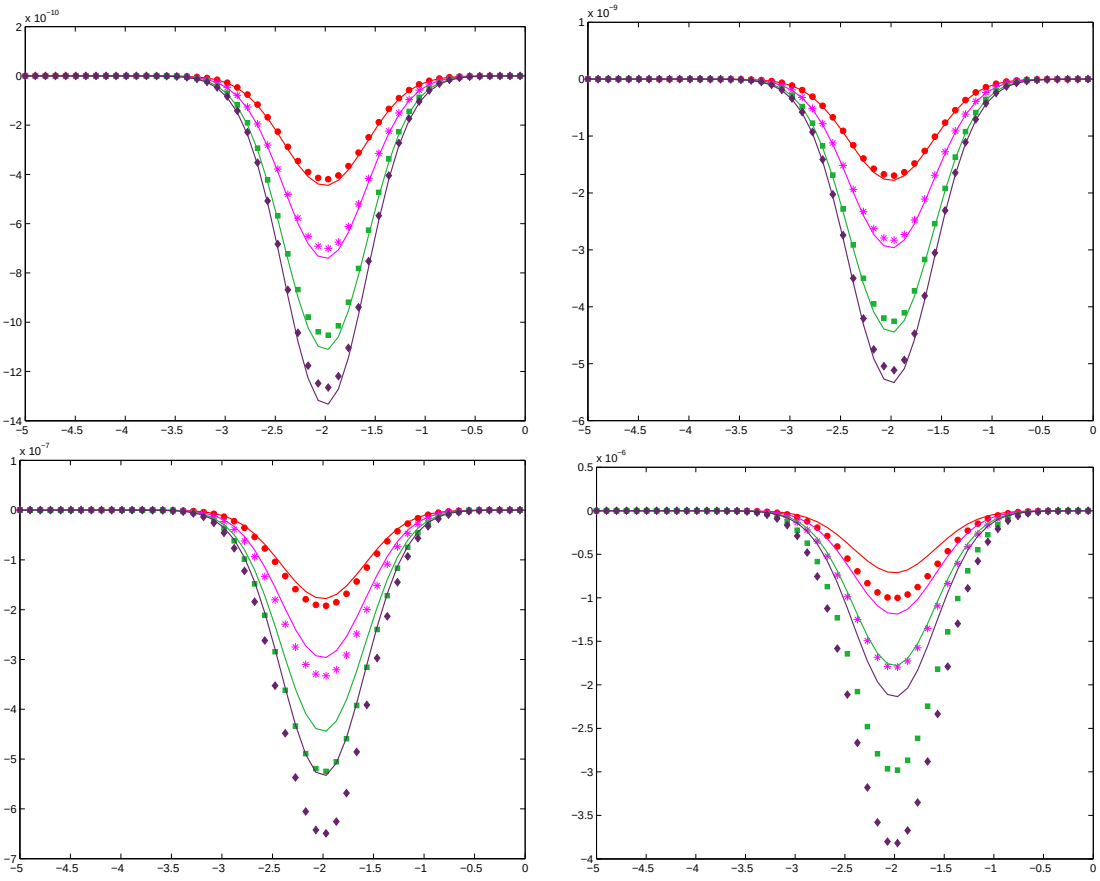

Figure 2.3: Validation of the asymptotic expansion formula for inclusions with different radius and thermal conductivities. From top to bottom, from left to right: the radius of the inclusion is 0.005, 0.01, 0.1 and 0.2. In each figure, the conductivities are from the top to the bottom: $1, 5, 2, 3$, and 4.

Figure 2.4 shows that the extrema of $I_\phi(T)$ correspond to the x_1 components of the locations of the anomalies.

Once the x_1 components, $z_j^1, j = 1, \ldots, m$, are found, in order to recover the x_2 components we minimize over $z_j^2 < 0, j = 1, \ldots, m$, the following functional

$$\left| I_\phi(T) - \epsilon^2 \sum_{j=1}^{m} \left(\frac{k_j}{k_0} - 1 \right) \int_0^T \nabla u_0((z_j^1, z_j^2), t) M^{(j)} \nabla \phi((z_j^1, z_j^2), t) dt \right|.$$

2.6.3 Ultrasonic Temperature Imaging

The principle of ultrasonic temperature imaging is to measure the local temperature near the anomaly. The aim is to reconstruct the anomaly with a better spatial and contrast

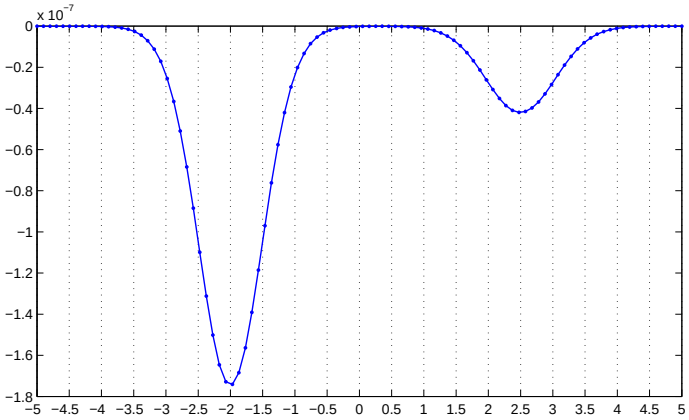

Figure 2.4: Reconstruction of the anomalies

resolutions than from boundary measurements. Theorem 2.5.1 says that

$$(u_\epsilon - u_0)(x,t) \approx -\epsilon \sum_{i=1}^{2} \partial_{x_i} u_0(z_{j_0},t)\psi_{j,i}\Big(\frac{x-z_{j_0}}{\epsilon}\Big),$$

for $|x - z_{j_0}| = O(\epsilon)$. Fix ω to be a window around the anomaly j_0. To reconstruct the shape and the thermal conductivity of this anomaly, a natural way would be to minimize over ϵB and k the functional

$$\int_0^T \int_\omega \Big|(u_\epsilon - u_0)(x,t) + \epsilon \sum_{i=1}^{2} \partial_{x_i} u_0(z_{j_0},t)\psi_{j,i}\Big(\frac{x-z_{j_0}}{\epsilon}\Big)\Big|^2 dxdt.$$

Standard regularization techniques can be used for solving this optimization problem. See [5].

2.7 Appendix

We derive equations (2.51)-(2.53) from (2.50), if f_2 is in $L^2((0,T)\times\mathbb{R})$ and

$$\lim_{\epsilon\to 0} \int_{0\le s\le\epsilon} \int_{|y|\le\epsilon} |f_2(x+y,t-s) - f_2(x,t)|dyds = 0. \tag{2.73}$$

Equation (2.51) is clear by dominated convergence. Equation (2.53) can be obtained for any $x_2 < 0$ by applying Cauchy Schwartz inequality and letting t tend to 0.
To obtain (2.52), first assume that f_2 is equal to the constant 1 in the neighborhood of (x_1,t) defined by $|\xi_1 - x_1| < \eta, |s-t| < \eta$. We observe the following, due to the boundary condition for G_2 away from singularities,

$$\lim_{x_2\to 0} (\partial_{x_2}\cdot + \cdot)\left(\iint_X f_2(\xi_1,s)G_2(x_1,x_2,\xi_1,t-s)d\xi_1 ds\right) = 0,$$

where X is the complement in $(0,t)\times\mathbb{R}$ of $(t-\eta,t)\times(x_1-\eta,x_1+\eta)$. Next we set for $x_2<0$, $u=\xi_1-x_1$, $r=s-t$. We want to determine

$$\lim_{x_2\to 0}(\partial_{x_2}\cdot+\cdot)\left(\int_0^\eta\int_{-\eta}^\eta G_2(u,x_2,0,r)dudr\right).$$

As

$$G_2(u,x_2,0,r)=\frac{1}{2\pi r}e^{-\frac{u^2}{4r}}\left[e^{-\frac{x_2^2}{4r}}+\sqrt{\pi r}e^{-x_2+r}\left(\operatorname{erf}\left(\frac{-x_2+2r}{2\sqrt{r}}\right)-1\right)\right],$$

integrating in u,

$$\int_{-\eta}^\eta G_2(u,x_2,0,r)du=\frac{1}{\sqrt{\pi r}}\operatorname{erf}\left(\frac{\eta}{2\sqrt{r}}\right)\left[e^{-\frac{x_2^2}{4r}}+\sqrt{\pi r}e^{-x_2+r}\left(\operatorname{erf}\left(\frac{-x_2+2r}{2\sqrt{r}}\right)-1\right)\right].$$

We can let x_2 tend to zero in the latter expression, since dominated convergence can be applied. Next, since

$$\partial_{x_2}G_2(u,x_2,0,r)=$$
$$\frac{1}{2\pi r}e^{-\frac{u^2}{4r}}\left[-\frac{x_2}{2r}e^{-\frac{x_2^2}{4r}}-\sqrt{\pi r}e^{-x_2+r}\left(\operatorname{erf}\left(\frac{-x_2+2r}{2\sqrt{r}}\right)-1\right)-e^{-x_2+r}e^{-\frac{(-x_2+2r)^2}{4r}}\right],$$

we notice that $\partial_{x_2}G_2(u,x_2,0,r)$ is the sum of three terms, the most singular is of order r^{-2}, the other two are of order, respectively, r^{-1} and $r^{-1/2}$. Starting with the most singular term, integrating in u,

$$-\int_{-\eta}^\eta\frac{x_2}{4\pi r^2}e^{-\frac{u^2+x_2^2}{4r}}du=-\frac{x_2}{2r\sqrt{\pi r}}e^{-\frac{x_2^2}{4r}}\operatorname{erf}\left(\frac{\eta}{2\sqrt{r}}\right).$$

To proceed with the integration in r, we make the substitution $r=\frac{x_2^2}{s^2}$ to obtain the integral

$$-\int_{x_2^2/\eta^2}^\infty\frac{1}{\sqrt{\pi}}e^{-\frac{s^2}{4}}\operatorname{erf}\left(\frac{s\eta}{2x_2}\right)ds.$$

By dominated convergence, the latter has the limit, as $x_2<0$ approaches 0,

$$\int_0^\infty\frac{1}{\sqrt{\pi}}e^{-\frac{s^2}{4}}ds=1.$$

We now examine the two terms from $\partial_{x_2}G_2(u,x_2,0,r)$, of lower order in r. Integrating in u,

$$-\int_{-\eta}^\eta\frac{1}{2\pi r}e^{-\frac{u^2}{4r}}\left[(\sqrt{\pi r}e^{-x_2+r}\left(\operatorname{erf}\left(\frac{-x_2+2r}{2\sqrt{r}}\right)-1\right)+e^{-x_2+r}e^{-\frac{(-x_2+2r)^2}{4r}}\right]du=$$
$$=\operatorname{erf}\left(\frac{\eta}{2\sqrt{r}}\right)\left[e^{-x_2+r}\left(\operatorname{erf}\left(\frac{-x_2+2r}{2\sqrt{r}}\right)-1\right)-\frac{1}{\sqrt{\pi r}}e^{-\frac{x_2^2}{4r}}\right]$$

We can let x_2 tend to zero in the latter expression, since dominated convergence can be applied. In conclusion,

$$\lim_{x_2\to 0}(\partial_{x_2}\cdot+\cdot)\left(\int_0^t\int_{-\infty}^\infty f_2(\xi_1,s)G_2(x_1,x_2,\xi_1,t-s)d\xi_1ds\right)=1,$$

if f_2 is equal to the constant 1 in some neighborhood of (x_1,t). The more general case can then be obtained by playing with inequalities, starting from estimate (2.73).

2.8 Concluding Remarks

In this chapter, starting from a realistic half space model for thermal imaging, we have developed a mathematical asymptotic analysis well suited for the design of reconstruction algorithms. Based on rigorously derived asymptotic estimates, after obtaining an approximation for the temperature profile, we were able to design noniterative detection algorithms. We have then presented numerical simulations to test them. We have also touched upon the subject of ultrasonic temperature imaging used for guiding in the course of thermal ablation therapy. Related optimization algorithms will be the subject of forthcoming work.

Chapter 3

Electrical Impedance Endo-Tomography

3.1 Introduction

Electrical impedance tomography (EIT) tries to recover the electrical conductivity distribution inside the body from measurements of current flows and voltages on its surface. It characterizes the change in measured impedance resulting from the conductivity change in a given volume element. The injected current concentrates at electrodes near the source and spreads throughout the whole conducting body, so that the injected current density decreases for increasing distance to electrodes. This feature makes it difficult to obtain accurate images of small and deep organs in the human body using EIT.

Electrical Impedance Endo-Tomography (EIET) is a new alternative method for scanning the conductivity of deep tissues or organs using an impedance probe placed at the center of the region of interest. The probe consists of electrodes placed at the surface of an insulating cylinder and spreads in the medium surrounding the probe. The electrodes are surrounded by the medium to be examined instead of encircling it. This new method has been developed for prostate imaging by Jossinet and his group [18, 19]. The basic assumption is that normal prostate tissue and tumor tissue have different electrical conductivity.

In practice captured current-voltage pairs must be limited by the number of electrodes attached on the surface of the probe, which restrict the resolution of the image. See [16]. Definitely, we can increase the resolution of the conductivity image by increasing the number of electrodes. However, it should be noticed that, beyond a certain level, increasing numbers of electrodes may not give any help for producing a better image for the inner-region of the body if we take account of inevitable noise in measurements and the inherent insensitivity mentioned before. In its most general form EIET is severely ill-posed and nonlinear. These major and fundamental difficulties can be understood by means of the mean value type theorem in elliptic partial differential equations. The value of the voltage potential at each point in the medium surrounding the probe can be expressed as a

weighted average of its neighborhood potential where the weight is determined by the conductivity distribution. In this weighted averaging way, the conductivity distribution is conveyed to the probe potential. Therefore, the probe data is entangled in the global structure of the conductivity distribution in a highly nonlinear way. This is the main obstacle to finding non-iterative reconstruction algorithms with limited data. If, however, we have additional structural information about the medium in advance, then we may be able to determine specific features about the conductivity distribution with good resolution. One such type of knowledge could be that the body surrounding the probe consists of a smooth background containing a number of unknown small inclusions with a significantly different conductivity. This situation arises for example in prostate cancer imaging.

In this case EIET seeks to recover the unknown inclusions. Due to the smallness of the inclusions the associated voltage potentials measured on the surface of the probe are very close to the potentials corresponding to the medium without inclusion. So unless one knows exactly what patterns to look for, noise will largely dominate the information contained in the measured data. Furthermore, in prostate imaging it is often not necessary to reconstruct the precise values of the conductivity or geometry of the inclusions. The information of real interest is their positions and size.

Since the situation of the electrodes in EIET, in the middle of the region of interest, creates a situation differing from classical EIT, the major classical concepts of EIT and accurate reconstruction techniques need to be revised and adapted to this new situation.

In [38], an asymptotic formula for the voltage perturbations on the probe that are due to the presence of a small anomaly has been derived as the size of the anomaly goes to zero. Based on that formula, a reconstruction method for some features of the anomaly has been proposed. This method enables detection of a single anomaly and its polarization tensor. However, it is impossible to extract information about the material property, such as conductivity and anisotropy, of the inclusion from boundary measurements.

In this chapter, our aims are threefold:

(i) We first find an isotropic inclusion of elliptic form with isotropic conductivity first-order polarization tensor of which coincides with the anisotropic one of a disk-shaped anisotropic inclusion. We then show how to extract anisotropy from higher-order anisotropic polarization tensors.

(ii) We also generalize the recent approach of conductivity imaging by elastic deformation to EIET and demonstrate its feasibility. This approach, called impediography, is based on the simultaneous measurement of a potential and of acoustic vibrations induced by ultrasound waves. Its intrinsic resolution depends on the size of the focal spot of the acoustic perturbation, and thus it provides high resolution images. The core idea of impediography is to extract more information about the conductivity from data that has been enriched by coupling the electric measurements to localized elastic perturbations. More precisely, one perturbs the medium during the electric measurements, by focusing ultrasonic waves on regions of small diameter inside the

body. Using a simple model for the mechanical effects of the ultrasound waves, one can show that the difference between the measurements in the unperturbed and perturbed configurations is asymptotically equal to the pointwise value of the energy density at the center of the perturbed zone. In practice, the ultrasounds impact a zone of a few millimeters in diameter. The perturbation should thus be sensitive to conductivity variations at the millimeter scale, which is the precision required for prostate cancer diagnostic.

(iii) Finally, we present a method for detecting multiple anomalies using a realistic electrode model.

3.2 Mathematical Model

Let Ω be a bounded domain in $\mathbb{R}^2$, with a connected smooth boundary $\partial\Omega$. Let ν denote the unit outward normal to $\partial\Omega$.

Introduce the weighted Sobolev space $W^{1,2}(\mathbb{R}^2 \setminus \overline{\Omega})$ of functions

$$\left\{ \frac{f(x)}{\sqrt{1+|x|^2}\ln(2+|x|^2)} \in L^2(\mathbb{R}^2 \setminus \overline{\Omega}) \ , \ \nabla f \in L^2(\mathbb{R}^2 \setminus \overline{\Omega}) \right\} .$$

$W^{1,2}(\mathbb{R}^2 \setminus \overline{\Omega})$ is a Hilbert space under the scalar product

$$(u,v) = \int_{\mathbb{R}^2\setminus\overline{\Omega}} \frac{u(x)v(x)}{(1+|x|^2)(\ln(2+|x|^2))^2}\, dx + \int_{\mathbb{R}^2\setminus\overline{\Omega}} \nabla u(x)\cdot\nabla v(x)\, dx \ .$$

Let $\mathcal{P}_0$ denote the set of constant functions on $\mathbb{R}^2$. We recall the Poincaré-type inequality

$$\int_{\mathbb{R}^2\setminus\overline{\Omega}} \frac{|u(x)|^2}{(1+|x|^2)(\ln(2+|x|^2))^2}\, dx \le C \int_{\mathbb{R}^2\setminus\overline{\Omega}} |\nabla u(x)|^2\, dx \ , \tag{3.1}$$

holds for all u in the quotient space $W^{1,2}(\mathbb{R}^2 \setminus \overline{\Omega})/\mathcal{P}_0$.

Suppose that $\mathbb{R}^2\setminus\overline{\Omega}$ contains a finite number m of small inhomogeneities D_s, $s=1,\dots,m$, each of the form $D_s = \epsilon B_s + z_s$, where B_s, $s=1,\dots,m$, is a bounded smooth domain in $\mathbb{R}^2$ containing the origin and $z_s \in \mathbb{R}^2 \setminus \overline{\Omega}$. We assume that the domains D_s, $s=1,\dots,m$ are separated from each other and from the boundary $\partial\Omega$. More precisely, we assume that there exists a constant $c_0 > 0$ such that

$$|z_s - z_{s'}| \ge 2c_0 > 0 \quad \forall\ s \ne s' \quad \text{and} \quad \operatorname{dist}(z_s, \partial\Omega) \ge 2c_0 > 0 \quad \forall\ s \ , \tag{3.2}$$

that ϵ, the common order of magnitude of the diameters of the inhomogeneities, is sufficiently small and that these inhomogeneities are disjoint. We also assume that the "background" $\mathbb{R}^2 \setminus \overline{\Omega}$ is homogeneous with conductivity 1 and the inhomogeneity D_s has conductivity k_s, $0 < k_s \ne 1 < +\infty$, for $1 \le s \le m$.

Let the function g represent the applied boundary current. We assume that it belongs to $L^2(\partial\Omega)$ and has mean value zero. Let u denote the steady-state voltage potential in the presence of the conductivity inhomogeneities $\bigcup_{s=1}^m D_s$, *i.e.*, the solution in $W^{1,2}(\mathbb{R}^2 \setminus \overline{\Omega})/\mathcal{P}_0$ to

$$\begin{cases} \nabla \cdot \left(\chi\left(\Omega \setminus \bigcup_{s=1}^m \overline{D}_s \right) + \sum_{s=1}^m k_s \chi(D_s) \right) \nabla u = 0 & \text{in } \mathbb{R}^2 \setminus \overline{\Omega}, \\ \left. \dfrac{\partial u}{\partial \nu} \right|_{\partial\Omega} = g, \quad \displaystyle\int_{\partial\Omega} g = 0, & \\ u(x) = O\Big(\dfrac{1}{|x|}\Big) & \text{as } |x| \to +\infty. \end{cases} \tag{3.3}$$

Let U denote the "background" potential, that is, the solution in $W^{1,2}(\mathbb{R}^2 \setminus \overline{\Omega})/\mathcal{P}_0$ to

$$\begin{cases} \Delta U = 0 & \text{in } \mathbb{R}^2 \setminus \overline{\Omega}, \\ \left. \dfrac{\partial U}{\partial \nu} \right|_{\partial\Omega} = g, \quad \displaystyle\int_{\partial\Omega} g = 0, & \\ U(x) = O\Big(\dfrac{1}{|x|}\Big) & \text{as } |x| \to +\infty. \end{cases} \tag{3.4}$$

The EIET technique is to detect unknown inclusions D_s, $s = 1, \ldots, m$, by means of a finite number of current-to-voltage pairs $(g, u|_{\partial\Omega})$ measured on $\partial\Omega$.

In [38], the following formula has been derived

$$\mathcal{S}_\Omega(u - U)(x) = -\epsilon^2 \nabla U(z) M(k, B) \nabla \Gamma(x, z) + o(\epsilon^2), \tag{3.5}$$

uniformly on $\partial\Omega$, where M is the polarization tensor associated with B and k and Γ is the fundamental solution to the Laplacian. $\mathcal{S}_\Omega$ is the single layer potential defined by

$$\mathcal{S}_\Omega \phi(x) = \int_{\partial\Omega} \Gamma(x, y) \phi(y)\, d\sigma(y), \quad \phi \in L^2(\partial\Omega),$$

and the polarization tensor M is given by

$$M(k, B) := \int_{\partial B} \Big(\frac{k+1}{2(k-1)} I - \mathcal{K}_\Omega^*\Big)^{-1}(\nu) y d\sigma(y),$$

where

$$\mathcal{K}_B^* \phi(x) = \int_{\partial B} \frac{\langle x - y, \nu_x \rangle}{2\pi |x - y|^2} \phi(y)\, d\sigma(y), \quad \phi \in L^2(\partial B).$$

It is not difficult to generalize formula (3.5) to the case where the anomaly has anisotropic conductivity. It suffices to replace M by the anisotropic polarization associated with B and its anisotropic conductivity matrix. It is known that detection of anisotropy can discriminate malignant tumors from benign ones.

Formula (3.5) says that the only information that can be reconstructed is $M(k, B)$. Since M is a mixture of volume and conductivity, it is then impossible to extract from boundary measurements material properties of the anomaly.

3.3 Detection of Anisotropy

3.3.1 Green's Function, Single and Double Layer Potentials

Let A be a positive-definite symmetric matrix. A *fundamental solution* or a *Green's function* $\Gamma^A(x,z)$ of the operator $\nabla_x \cdot A\nabla_x$ is the solution to

$$\nabla_x \cdot A\nabla_x \Gamma^A(x,z) = \delta(x-z), \tag{3.6}$$

where δ is Dirac's delta function.

Let A_* be the positive-definite symmetric matrix such that $A^{-1} = A_*^2$. A Green's function $\Gamma^A(x,z)$ is given by

$$\Gamma^A(x,z) = \Gamma^A(x-z) = \begin{cases} \frac{1}{2\pi\sqrt{|A|}} \ln ||A_*(x-z)||, & \text{if } d=2 \\ -\frac{1}{4\pi\sqrt{|A|}} \frac{1}{||A_*(x-z)||}, & \text{if } d=3 \end{cases}, \tag{3.7}$$

where $|A|$ is the determinant of A and $||\cdot||$ is the Euclidean norm of the vector in $\mathbb{R}^d$.

Let D be a bounded smooth domain in $\mathbb{R}^d$, the *single* and *double layer potentials* associated with A of the density function $\phi \in L^2(\partial D)$ are respectively defined by

$$\mathcal{S}_D^A \phi(x) = \int_{\partial D} \Gamma^A(x-y)\phi(y) d\sigma(y), \quad x \in \mathbb{R}^d \tag{3.8}$$

and

$$\mathcal{D}_D^A \phi(x) = \int_{\partial D} \nu_y \cdot A\nabla\Gamma^A(x-y)\phi(y) d\sigma(y), \quad x \in \mathbb{R}^d \setminus \partial D. \tag{3.9}$$

The *jump relations* obeyed by the double layer potential and by the normal derivative of the single layer potential for $x \in \partial D$ are

$$\nu_x \cdot A\nabla\mathcal{S}_D^A\phi(x)\big|_+ - \nu_x \cdot A\nabla\mathcal{S}_D^A\phi(x)\big|_- = \phi(x), \tag{3.10}$$

$$\mathcal{D}_D^A\phi(x)\big|_+ - \mathcal{D}_D^A\phi(x)\big|_- = -\phi(x). \tag{3.11}$$

3.3.2 Anisotropic Polarization Tensors

We now recall the definition and some important properties of the (generalized) *anisotropic polarization tensors* (APT's) associated with an anisotropic inclusion embedded in an anisotropic background.

Let D be a bounded smooth domain in $\mathbb{R}^d$, $d = 2, 3$. Suppose that the conductivity of D is $\widetilde{A}$ and that of $\mathbb{R}^d \setminus \bar{D}$ is A, where A and $\widetilde{A}$ are constant $d \times d$ positive-definite symmetric matrix with $A \neq \widetilde{A}$. The matrix $\widetilde{A} - A$ is assumed to be either positive-definite or negative-definite.

We will use the standard notations for *multi-indices*: for a multi-index $\alpha = (\alpha_1, \ldots, \alpha_d) \in \mathbb{N}^d$, let $x^\alpha = x_1^{\alpha_1} \cdots x_d^{\alpha_d}$ and $|\alpha| = \alpha_1 + \cdots + \alpha_d$.

Define the anisotropic polarization tensors (APT) [7], as follows:

Definition 3.3.1 *For a multi-index $\alpha \in \mathbb{N}^d$ with $|\alpha| \geq 1$, let $(f_\alpha, g_\alpha) \in L^2(\partial D) \times L^2(\partial D)$ be the unique solution to*

$$\begin{cases} \mathcal{S}_D^{\widetilde{A}} f_\alpha - \mathcal{S}_D^A g_\alpha = x^\alpha \\ \nu \cdot \widetilde{A} \nabla \mathcal{S}_D^{\widetilde{A}} f_\alpha\big|_- - \nu \cdot A \nabla \mathcal{S}_D^A g_\alpha\big|_+ = \nu \cdot A \nabla x^\alpha \end{cases} \quad \text{on } \partial D. \tag{3.12}$$

For a pair of multi-indices $\alpha, \beta \in \mathbb{N}^d$, define the generalized anisotropic polarization tensors associated with the domain D and anisotropic conductivities A and $\widetilde{A}$, by:

$$M_{\alpha\beta}(A, \widetilde{A}, D) = \int_{\partial D} x^\beta g_\alpha(x) d\sigma(x). \tag{3.13}$$

If $|\alpha| = |\beta| = 1$, it means that when $\alpha = e_i$ and $\beta = e_j$ for $i, j = 1, \ldots, d$, where $\{e_k\}_k$ is the standard basis for $\mathbb{R}^d$, we denote $M_{\alpha\beta}$ by M_{ij}.

We note that the first-order APT was first introduced in [20] and it is proved there that M_{ij} is symmetric and positive (negative, resp.) definite if $\widetilde{A} - A$ is positive (negative, resp.) definite. The generalized APT's enjoy the same properties [7].

For a multi-index $\alpha \in \mathbb{N}^d$ with $|\alpha| \geq 1$, let:

$$\theta_\alpha(x) = \chi(D) \mathcal{S}_D^{\widetilde{A}} f_\alpha(x) + \chi(\mathbb{R}^d \setminus D) \mathcal{S}_D^A g_\alpha(x). \tag{3.14}$$

Then θ_α is the solution to the following transmission problem:

$$\begin{cases} \nabla \cdot A \nabla \theta_\alpha = 0 & \text{in } \mathbb{R}^d \setminus \bar{D}, \\ \nabla \cdot \widetilde{A} \nabla \theta_\alpha = 0 & \text{in } D, \\ \theta_\alpha\big|_- - \theta_\alpha\big|_+ = x^\alpha & \text{on } \partial D, \\ \nu \cdot \widetilde{A} \nabla \theta_\alpha\big|_- - \nu \cdot A \nabla \theta_\alpha\big|_+ = \nu \cdot A \nabla x^\alpha & \text{on } \partial D, \\ \theta_\alpha(x) \to 0, & \text{as } |x| \to \infty, \text{ if } d = 3, \\ \theta_\alpha(x) - \frac{1}{2\pi\sqrt{|A|}} \ln ||A_* x|| \int_{\partial D} \theta_\alpha(y) d\sigma(y) \to 0 & \text{as } |x| \to \infty, \text{ if } d = 2. \end{cases} \tag{3.15}$$

It then follows from the jump conditions (3.10) and (3.11) that for any pair of multi-

indices α and β,

$$M_{\alpha\beta} = \int_{\partial D} x^\beta g_\alpha d\sigma = \int_{\partial D} x^\beta \left(\nu \cdot A\nabla \mathcal{S}_D^A g_\alpha\big|_+ - \nu \cdot A\nabla \mathcal{S}_D^A g_\alpha\big|_-\right) d\sigma$$
$$= \int_{\partial D} x^\beta \left(\nu \cdot \widetilde{A}\nabla \mathcal{S}_D^{\widetilde{A}} f_\alpha\big|_- - \nu \cdot A\nabla x^\alpha\right) d\sigma - \int_{\partial D} \nu \cdot A\nabla x^\beta \left(\mathcal{S}_D^{\widetilde{A}} f_\alpha - x^\alpha\right) d\sigma$$
$$= \int_{\partial D} \left(\nu \cdot (\widetilde{A} - A)\nabla x^\beta\right) \theta_\alpha\big|_- d\sigma \quad (3.16)$$

3.3.3 Detection of First-Order APT

The aim of this section is to find an inclusion of elliptic form with isotropic conductivity first order polarization tensor of which coincides with the one of disk-shaped anisotropic inclusion.

We recall that the first order polarization tensor associated with the domain B, where B is a disk of radius d, of anisotropic conductivity $\widetilde{A}$ embedded in an isotropic background of conductivity I is given by

$$M_d(I, \widetilde{A}, B) = 2|B|(\widetilde{A} + I)^{-1}(\widetilde{A} - I), \quad (3.17)$$

where $|B| = \pi d^2$.

Let $\mathcal{E}'$ be an ellipse whose semi-axes are on the x_1 and x_2 axes and of the length a and b, respectively. Let $B = R\mathcal{E}'$, where R is an orthogonal matrix ($RR^T = I$). We recall that the polarization tensor associated with the elliptic inclusion B of isotropic conductivity kI embedded in an isotropic background of conductivity I is given by

$$M_e(I, \widetilde{A}, B) = (k-1)|B|R \begin{pmatrix} \frac{a+b}{a+kb} & 0 \\ 0 & \frac{a+b}{b+ka} \end{pmatrix} R^T, \quad (3.18)$$

where $|B| = \pi ab$.

At this point let us review a method to recover a, b, k and R form a given first order polarization tensor M_d. We suppose that the elliptic and disk-shaped inclusions have the same known volume:

$$|B| = \pi ab = \pi d^2. \quad (3.19)$$

The equivalence of the first order of APT (3.17) and (3.18), implies the following equality

$$\frac{1}{|B|}\mathrm{tr}(M_e^{-1}) = \frac{1}{|B|}\mathrm{tr}(M_d^{-1}) = \frac{k+1}{k-1}. \quad (3.20)$$

Then, if we introduce the notation

$$tr = \mathrm{tr}((|B|\widetilde{A} - |B|I)^{-1}(|B|\widetilde{A} + |B|I)), \quad (3.21)$$

we have

$$k = \frac{tr+1}{tr-1}. \tag{3.22}$$

Let λ_1 and λ_2 denote the eigenvalues of the matrix $2(|B|\widetilde{A}+|B|I)^{-1}(|B|\widetilde{A}-|B|I)$:

$$\begin{cases} \lambda_1 = (k-1)\frac{a+b}{a+kb}, \\ \lambda_2 = (k-1)\frac{a+b}{b+ka}. \end{cases} \tag{3.23}$$

It is easy to see that

$$(k-1)(a+b) = \lambda_1(a+kb) = \lambda_2(b+ka), \tag{3.24}$$

or equivalently,

$$\lambda_1(a^2\pi + k|B|) = \lambda_2(ka^2\pi + |B|). \tag{3.25}$$

The lengths a and b can be recovered by

$$a = \sqrt{\frac{|B|}{\pi}}\sqrt{\frac{\lambda_2 - k\lambda_1}{\lambda_1 - k\lambda_2}} \tag{3.26}$$

and

$$b = \sqrt{\frac{|B|}{\pi}}\sqrt{\frac{\lambda_1 - k\lambda_2}{\lambda_2 - k\lambda_1}}. \tag{3.27}$$

Finally, R can be computed by solving a linear system of equations. It is a function of the directions of anisotropy of A.

3.3.4 APT for Ellipses

Let D be a bounded smooth domain in $\mathbb{R}^2$ whose conductivity is given by 2×2 positive-definite symmetric matrix γ. Let the background conductivity be given by I. For a multi-index α with $|\alpha| \geq 1$, let

$$M_\alpha = \begin{pmatrix} M_{\alpha 1} \\ M_{\alpha 2} \end{pmatrix} \tag{3.28}$$

be the (higher-order) anisotropic polarization tensor. Let

$$X_\alpha = \begin{pmatrix} X_{\alpha 1} \\ X_{\alpha 2} \end{pmatrix} \tag{3.29}$$

be the vector defined by

$$X_{\alpha j} = \int_D \nabla y^\alpha \cdot (\gamma - I)\mathbf{e}_j dy, \quad j = 1, 2, \tag{3.30}$$

where $\{\mathbf{e}_j\}_{j=1,2}$ is an orthonormal basis in $\mathbb{R}^2$.

Let D be an ellipse such that $D = R_\psi(D')$ for some rotation:

$$R_\psi = \begin{pmatrix} \cos\psi & -\sin\psi \\ \sin\psi & \cos\psi \end{pmatrix} \tag{3.31}$$

and an ellipse D' of the form

$$\frac{x^2}{p^2} + \frac{y^2}{q^2} = 1, \quad (p \geq q). \tag{3.32}$$

Let $m = \frac{p-q}{p+q}$ and

$$J = \begin{pmatrix} 1 & 0 \\ 0 & -1 \end{pmatrix}. \tag{3.33}$$

Then, the following formula for M_α for ellipses was obtained in [21]:

$$M_\alpha = 2\Big[(\gamma + I) - m(\gamma - I)R_\psi J R_\psi^T\Big]^{-1} X_\alpha. \tag{3.34}$$

In particular, the first-order APT $M = (M_{jk})$ is given by

$$M = 2\Big[(\gamma+I)-m(\gamma-I)R_\psi J R_\psi^T\Big]^{-1}(\gamma-I) = 2|D|\Big[(\gamma-I)^{-1}(\gamma+I)-mR_\psi J R_\psi^T\Big]^{-1}. \tag{3.35}$$

Moreover, $M^{-1}M_\alpha$ is given by

$$M^{-1}M_\alpha = \frac{1}{|D|}(\gamma - I)^{-1} X_\alpha. \tag{3.36}$$

3.3.5 Anisotropy Detection

We prove now that the use of higher-order polarization tensors yields the reconstruction of the material property of the anomaly.

For multi-index α, such as $|\alpha| = 3$, we have the four possible cases presented in table 3.1

where T_j is given by

$$T_j = \int_D y_j^2 dy. \tag{3.37}$$

To calculate T_j, we introduce the elliptic coordinates (r, ϕ). In these coordinates, the ellipse D' is given by

$$D' = \left\{ \begin{pmatrix} y_1 \\ y_2 \end{pmatrix} = \begin{pmatrix} pr\cos\phi \\ qr\sin\phi \end{pmatrix} \middle| \, 0 \leq r \leq 1, 0 \leq \phi < 2\pi \right\}, \tag{3.38}$$

and the ellipse D is given by

$$D = \left\{ \begin{pmatrix} y_1 \\ y_2 \end{pmatrix} = \begin{pmatrix} pr\cos\phi\cos\psi - qr\sin\phi\sin\psi \\ pr\cos\phi\sin\psi + qr\sin\phi\cos\psi \end{pmatrix} \middle| \, 0 \leq r \leq 1, 0 \leq \phi < 2\pi \right\}. \tag{3.39}$$

α	y^α	∇y^α	$X_{\alpha j}$	$M^{-1}M_\alpha$
$(3,0)$	y_1^3	$\begin{pmatrix} 3y_1^2 \\ 0 \end{pmatrix}$	$3(\gamma - I)_{1j}T_1$	$\frac{3T_1}{\lvert D\rvert}\begin{pmatrix} 1 \\ 0 \end{pmatrix}$
$(2,1)$	$y_1^2 y_2$	$\begin{pmatrix} 2y_1y_2 \\ y_1^2 \end{pmatrix}$	$(\gamma - I)_{2j}T_1$	$\frac{T_1}{\lvert D\rvert}\begin{pmatrix} 0 \\ 1 \end{pmatrix}$
$(1,2)$	$y_1 y_2^2$	$\begin{pmatrix} y_2^2 \\ 2y_1y_2 \end{pmatrix}$	$(\gamma - I)_{1j}T_2$	$\frac{T_2}{\lvert D\rvert}\begin{pmatrix} 1 \\ 0 \end{pmatrix}$
$(0,3)$	y_2^3	$\begin{pmatrix} 0 \\ 3y_1^2 \end{pmatrix}$	$3(\gamma - I)_{2j}T_2$	$\frac{3T_2}{\lvert D\rvert}\begin{pmatrix} 0 \\ 1 \end{pmatrix}$

Table 3.1: Possible cases for $|\alpha| = 3$.

The Jacobian is given by

$$\begin{aligned}\frac{D(y_1,y_2)}{D(r,\phi)} &= \det\begin{vmatrix} \frac{\partial y_1}{\partial r} & \frac{\partial y_1}{\partial \phi} \\ \frac{\partial y_2}{\partial r} & \frac{\partial y_2}{\partial \phi} \end{vmatrix} \\ &= \det\begin{vmatrix} p\cos\phi\cos\psi - q\sin\phi\sin\psi & -pr\sin\phi\cos\psi - qr\cos\phi\sin\psi \\ p\cos\phi\sin\psi + q\sin\phi\cos\psi & -pr\sin\phi\sin\psi + qr\cos\phi\cos\psi \end{vmatrix} = abr. \quad (3.40)\end{aligned}$$

Using the elliptic coordinates, we have

$$\begin{aligned}T_1 &= \int_D y_1^2 dy_1 dy_2 = \int_D (pr\cos\phi\cos\psi - qr\sin\phi\sin\psi)^2 \frac{D(y_1,y_2)}{D(r,\phi)} dr d\phi \\ &= pq\int_0^1 r^3 dr \int_0^{2\pi} (p^2\cos^2\phi\cos^2\psi + q^2\sin^2\phi\sin^2\psi - 2pq\cos\phi\sin\phi\cos\psi\sin\psi) d\psi \\ &= \frac{\pi pq}{4}(p^2\cos^2\psi + q^2\sin^2\psi) = \frac{|D|}{4}(p^2\cos^2\psi + q^2\sin^2\psi). \quad (3.41)\end{aligned}$$

Similarly, we obtain

$$T_2 = \int_D y_2^2 dy_1 dy_2 = \frac{\pi pq}{4}(p^2\sin^2\psi + q^2\cos^2\psi) = \frac{|D|}{4}(p^2\sin^2\psi + q^2\cos^2\psi). \quad (3.42)$$

Let z, M and M_α be the detected location, the first-order and the higher-order ($|\alpha| = 3$) APTs. Suppose that the ellipse B is small such as $\epsilon^2 = pq$.

Using the expression of $M^{-1}M_\alpha$ we find

$$4\frac{T_1}{|D|} = p^2\cos^2\psi + q^2\sin^2\psi, \quad (3.43)$$

$$4\frac{T_2}{|D|} = p^2\sin^2\psi + q^2\cos^2\psi. \quad (3.44)$$

It is easy to see that p and q can be computed as the roots of the following equation:

$$\xi^2 - \xi\sqrt{4\frac{T_1}{|D|} + 4\frac{T_2}{|D|} + 2\epsilon^2} + \epsilon^2 = 0. \tag{3.45}$$

Indeed, the expression under the sing of square root is equal to

$$4\frac{T_1}{|D|} + 4\frac{T_2}{|D|} + 2\epsilon^2 = p^2(\cos^2\psi + \sin^2\psi) + q^2(\cos^2\psi + \sin^2\psi) + 2pq = (p+q)^2. \tag{3.46}$$

Once p and q are found, ψ is recovered by

$$\psi = \frac{1}{2}\arccos\left(\frac{4\frac{T_1}{|D|} - 4\frac{T_2}{|D|}}{p^2 - q^2}\right) \tag{3.47}$$

since

$$4\frac{T_1}{|D|} - 4\frac{T_2}{|D|} = (p^2 - q^2)(\cos^2\psi - \sin^2\psi) = (p^2 - q^2)\cos(2\psi). \tag{3.48}$$

Finally, using the representation (3.35), we can find the conductivity matrix γ using the following formula:

$$\gamma = \left[2\pi\epsilon^2 M^{-1} + mR_\psi J R_\psi^T + I\right]\left[2\pi\epsilon^2 M^{-1} + mR_\psi J R_\psi^T - I\right]^{-1}. \tag{3.49}$$

3.3.6 Numerical Tests

We provide results for anisotropy detection in the presence of noise. In all of these numerical tests we have used the following parameters

$$q = 1.5, \tag{3.50}$$
$$p = 2.5, \tag{3.51}$$
$$\psi = \frac{\pi}{6} \simeq 0.5236, \tag{3.52}$$
$$\gamma = \begin{pmatrix} 3 & 1 \\ 1 & 3 \end{pmatrix}. \tag{3.53}$$

To show the performance of the presented anisotropy detection method we apply to exact values of parameters multiplicative gaussian noises of variance σ^2:

$$\widetilde{\epsilon^2} = \epsilon^2(1 + \sigma g_\epsilon), \tag{3.54}$$
$$\widetilde{M} = \begin{pmatrix} M_{11}(1+\sigma g_{11}) & M_{12}(1+\sigma g_{12}) \\ M_{21}(1+\sigma g_{12}) & M_{22}(1+\sigma g_{22}) \end{pmatrix}, \tag{3.55}$$
$$\widetilde{T_1} = T_1(1 + \sigma g_1), \tag{3.56}$$
$$\widetilde{T_2} = T_2(1 + \sigma g_2), \tag{3.57}$$

where g_ϵ, g_1, g_2, g_{11}, g_{12} and g_{22} are independent gaussian random variables.

The results of numerical tests are presented in Table 3.2.

σ	q	p	ψ	γ
0	1.5	2.5	0.5236	$\begin{pmatrix} 3 & 1 \\ 1 & 3 \end{pmatrix}$
0.01	1.48	2.52	0.5382	$\begin{pmatrix} 2.92 & 0.97 \\ 0.97 & 2.92 \end{pmatrix}$
0.1	1.03	2.87	0.5838	$\begin{pmatrix} 3.13 & 0.7 \\ 0.7 & 3.13 \end{pmatrix}$
0.5	0.59	2.73	0.8187	$\begin{pmatrix} 4.31 & 6.24 \\ 6.24 & 4.31 \end{pmatrix}$

Table 3.2: Results of anisotropy detection.

3.4 EIET by Elastic Deformation

The aim of this section is to demonstrate the feasibility of the electrical impedance by elastic deformation (or impediography) for endo-tomography.

3.4.1 Physical Model

One or several currents are imposed on the surface $\partial\Omega$ and the induced potentials are measured on the boundary. At the same time, a circular region ω of a few millimeters in $\mathbb{R}^2 \setminus \overline{\Omega}$ is mechanically excited by ultrasonic waves, which dilate this region. The measurements are made as the focus of the ultrasounds scans an entire region around Ω. Several sets of measurements can be obtained by varying the ultrasound waves amplitudes and the applied currents.

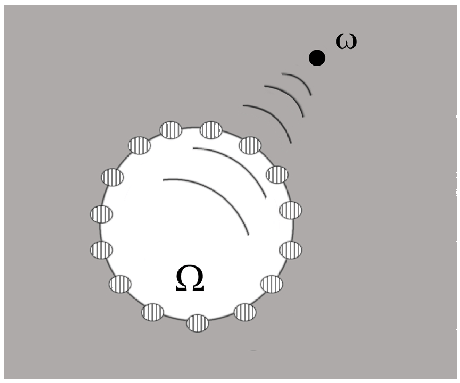

Figure 3.1: Experimental setup

We assume that the conductivity of each small disk B is proportional to its volume V_B

$$\gamma(x) = \rho(x)V_B,$$

where $\rho(x)$ is coefficient depending on the point $x \in \Omega$.

The ultrasonic waves induce a small elastic deformation of the disk B. If this deformation is isotropic, the material of points of B occupy a volume $\widetilde{V}_B$ in the perturbed configuration, which at first order is equal to

$$\widetilde{V}_B = V_B\bigg(1 + 2\frac{\Delta r}{r} + o(\Delta r)\bigg),$$

where r is the radius of the disk B and Δr is its variation due to the elastic perturbation. As a consequence, the perturbed conductivity is given by

$$\widetilde{\gamma}(x) = \eta(x)\gamma(x), \quad \text{for all } x \in \Omega, \tag{3.58}$$

where $\eta(x)$ is a known function.

3.4.2 Mathematical Model

Let us now formulate our problem. We suppose that the conductivity $\gamma(x)$ is known close to the boundary of domain Ω and is equal to a positive constant for $|x|$ large enough. We denote by u the voltage potential induced by a current g, in the absence of ultrasonic perturbations. It is given by

$$\begin{cases} \nabla_x \cdot (\gamma(x)\nabla_x u) = 0 & \text{in } \mathbb{R}^2 \setminus \overline{\Omega}, \\ \gamma(x)\frac{\partial u}{\partial \nu} = g & \text{on } \partial\Omega, \\ u(x) = O\big(\frac{1}{|x|}\big) & \text{as } |x| \to +\infty. \end{cases} \tag{3.59}$$

We denote by u_ω the voltage potential induced by a current g, in the presence of an ultrasonic perturbation localized in a disk domain $\omega = z + \delta B$ of volume $|\omega| = O(\delta^2)$. The voltage potential u_ω is a solution to

$$\begin{cases} \nabla_x \cdot (\gamma_\omega(x)\nabla_x u_\omega) = 0 & \text{in } \mathbb{R}^2 \setminus \overline{\Omega}, \\ \gamma(x)\frac{\partial u_\omega}{\partial \nu} = g & \text{on } \partial\Omega, \\ u_\omega(x) = O\big(\frac{1}{|x|}\big) & \text{as } |x| \to +\infty, \end{cases} \tag{3.60}$$

with the notation

$$\gamma_\omega(x) = \gamma(x)\big(1 + \mathbf{1}_\omega(x)(\eta(x) - 1)\big), \tag{3.61}$$

where $\mathbf{1}_\omega$ is the characteristic function of the domain ω.

As the zone deformed by the ultrasound wave is small, we can view it as a small volume perturbation of the background conductivity γ, and seek an asymptotic expansion of the boundary values of $u_\omega - u$. The method of small volume expansions shows that comparing u_ω and u on $\partial\Omega$ provides information about the conductivity.

Define $\{\zeta_\omega^i\}_{i=1}^d$ to be the solutions to

$$\begin{cases} \nabla \cdot (\gamma_\omega \nabla \zeta_\omega^i) = \nabla \cdot (\gamma \nabla x_i) & \text{in } \mathbb{R}^2 \setminus \overline{\Omega}, \\ \gamma_\omega \frac{\partial \zeta_\omega^i}{\partial \nu} = \gamma \nu_i & \text{on } \partial\Omega, \\ \zeta_\omega^i(x) = O\big(\frac{1}{|x|}\big), & \text{as } |x| \to +\infty. \end{cases} \tag{3.62}$$

Following exactly the same arguments as those in [3], we can prove that the following result holds.

Theorem 3.4.1 *Assume that $u \in W^{2,\infty}(\omega)$. Then,*

$$\int_{\partial\Omega}(u_\omega - u)gd\sigma = \int_\Omega(\gamma_\omega - \gamma)M_\omega\nabla u\cdot\nabla u dx + O(|\omega|^{1+\kappa}), \tag{3.63}$$

for some positive κ, where the matrix valued function $M_\omega(x)$ is given by

$$(M_\omega)_{jk} = -\frac{\partial\zeta_\omega^j}{\partial x_k}. \tag{3.64}$$

Moreover, in the case where ω is a disk, $M_\omega(x)$ is given by

$$M_\omega(x) = \frac{2}{\eta(x)+1}\mathbf{I}\mathrm{d}_2. \tag{3.65}$$

3.4.3 Conductivity Recovery

Suppose that $\omega(z)$ is a centered at z disk. The function $\mathcal{S}(z)$ is given by

$$\mathcal{S}(z) = \left(2\int_{\omega(z)}\frac{\eta(x)-1}{\eta(x)+1}dx\right)^{-1}\int_{\partial\Omega}(u_{\omega(z)} - u)gd\sigma \tag{3.66}$$

can be reconstructed from measurements on the boundary $\partial\Omega$. Theorem 3.4.1 shows that

$$\mathcal{S}(z) \approx \gamma(z)|\nabla u(z)|^2. \tag{3.67}$$

Let Ω_1 be a domain containing Ω. If we scan the region $\Omega_1 \setminus \overline{\Omega}$ then, in view of (3.67), we can replace the conductivity problem (3.59) by the following nonlinear system of equations:

$$\begin{cases} \nabla\cdot\left(\frac{\mathcal{S}(x)}{|\nabla u|^2}\nabla u\right) = 0 & \text{in } \Omega_1\setminus\overline{\Omega}, \\ \frac{\mathcal{S}(x)}{|\nabla u|^2}\frac{\partial u}{\partial\nu} = g & \text{on } \partial\Omega, \\ \nabla\cdot\gamma\nabla u = 0 & \text{in } \mathbb{R}^2\setminus\overline{\Omega_1}, \\ \frac{\mathcal{S}(x)}{|\nabla u|^2}\frac{\partial u}{\partial\nu}|_- = \gamma\frac{\partial u}{\partial\nu}|_+ & \text{on } \partial\Omega_1, \\ u(x) = O\left(\frac{1}{|x|}\right) & \text{as } |x|\to+\infty. \end{cases} \tag{3.68}$$

The solution of (3.68) can be found using the perturbative method described below.

One follows the following recursive procedure:

1. We start from an initial guess for the conductivity γ, and solve the corresponding Dirichlet conductivity problem

$$\begin{cases} \nabla \cdot (\gamma \nabla u_0) = 0 & \text{in } \mathbb{R}^2 \setminus \overline{\Omega}, \\ u_0 = \phi & \text{on } \partial\Omega, \\ u_0(x) = O\big(\frac{1}{|x|}\big) & \text{as } |x| \to +\infty, \end{cases} \tag{3.69}$$

   where $\phi = u$ on $\partial\Omega$ is the potential before any elastic perturbation. Well chosen initial guess permits to significantly reduce the number of necessary iterations for solving the problem (3.68).

   The discrepancy between the data and our guessed solution is

$$\epsilon_0 = \frac{\mathcal{S}(x)}{|\nabla u_0|^2} - \gamma_0. \tag{3.70}$$

2. We then introduce a corrector u_c computed as the solution to

$$\begin{cases} \nabla \cdot (\gamma \nabla u_c) = -\nabla \cdot (\epsilon_0 \nabla u_0) & \text{in } \Omega, \\ u_c = 0 & \text{on } \partial\Omega, \\ u_c(x) = O\big(\frac{1}{|x|}\big) & \text{as } |x| \to +\infty. \end{cases} \tag{3.71}$$

3. The conductivity correction is then given by

$$\gamma = \frac{\mathcal{S}(x) - 2\gamma \nabla u_c \cdot \nabla u_0}{|\nabla u_0|^2}. \tag{3.72}$$

4. We repeat these stages until the moment when the successive values of the conductivity γ became sufficiently close one to each other.

We now present a test for this iterative procedure. The conductivity distribution is presented in Figure 3.2. The background conductivity is 0.5, that of the elliptic inclusion is 0.85, that of the L is 2.55, and that of the triangle is 1.5.

The following simulations are done using the partial differential equation solver FreeFem++ [15]. Numerically, to solve the equations posed on unbounded domains we set the solutions to be 0 on some sphere of large radius containing Ω_1. This turns out to be provide good approximations of the solutions because of their behavior at infinity.

Figure 3.3 shows an initial guess, where

$$\gamma = \begin{cases} 1 & \text{if } 3 \leq |x| \leq 14, \\ 0.5 & \text{elsewhere.} \end{cases} \tag{3.73}$$

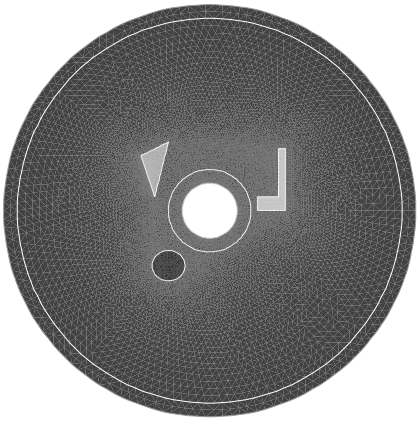

Figure 3.2: Conductivity distribution.

Figure 3.3: Initial guess.

Figure 3.4 shows the conductivity distribution reconstructed used only one g equals to $\frac{x_1}{|x|}$ on the left, or (on the right) $\frac{x_2}{|x|}$.

Figure 3.5 shows the reconstructed conductivity distribution obtained by using 4 currents $\frac{x_1}{|x|}$, $\frac{x_2}{|x|}$, $\frac{x_1+x_2}{\sqrt{2}|x|}$ and $\frac{x_1-x_2}{\sqrt{2}|x|}$, after one iteration (on the left) and 5 iterations (on the right).

3.5 Electrode Model

3.5.1 Physical Principles

Suppose that Ω is the disk of center the origin and radius R. Consider $n(=16)$ electrodes equidistantly placed at $\partial\Omega$. Suppose that the conductivity of the background is a positive

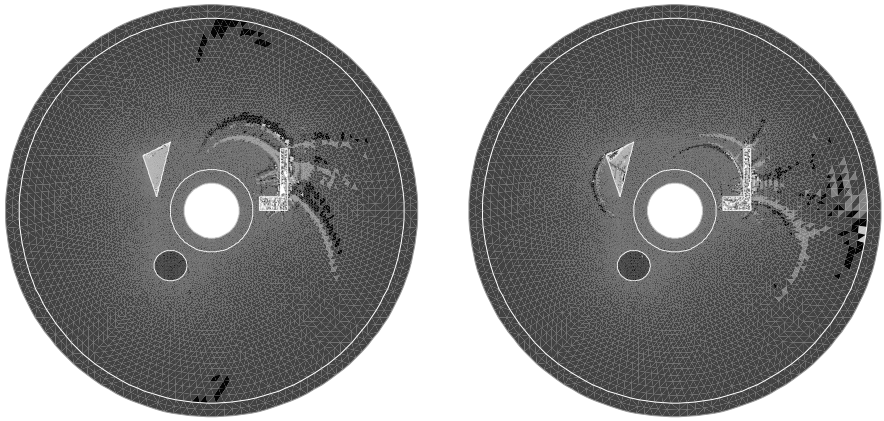

Figure 3.4: Conductivity distribution with one measurement after 200 iterations.

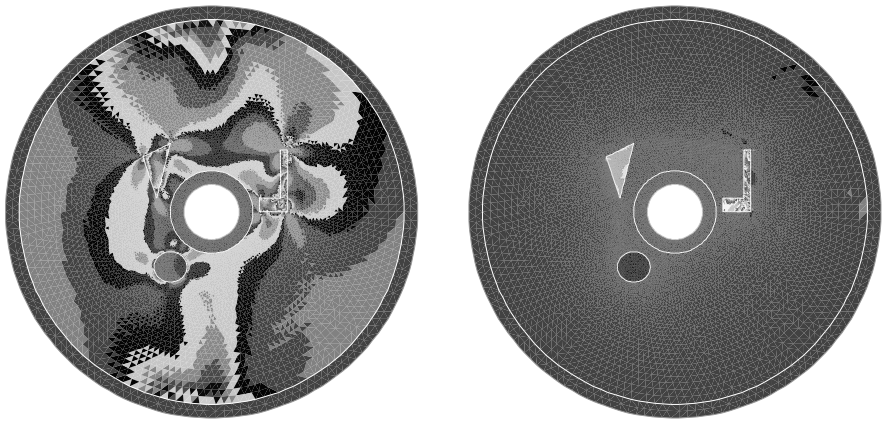

Figure 3.5: Conductivity distribution with multiple measurements and after only 1 (on the left) or 5 iterations (on the right).

constant σ_0. The measurements of the potential on the boundary is carried out using one pair of current injection and one pair of voltage sensing. We suppose that for the pair of current injection the electrodes are diametrically opposed and for the pair of voltage sensing the electrodes are neighbors. The pair of current injection is denoted by S and the one of voltage sensing by M.

Suppose that the conductivity of the anomaly is given by $\sigma_0 + \Delta\sigma$ and its volume by $\Delta\Omega$, where $\Delta\sigma$ and $\Delta\Omega$ satisfy

$$\Delta\sigma \ll \sigma_0 \qquad \text{et} \qquad |\Delta\Omega| \ll |\Omega|.$$

$$\Delta Z \simeq -\frac{\Delta\sigma|\Delta\Omega|}{\sigma_0^2}\vec{\jmath}_S(z)\cdot\vec{\jmath}_M(z),$$

where $z=(z_1,z_2)$ is the center of the anomaly and $\vec{\jmath}_S$ and $\vec{\jmath}_M$ are the current densities created in the absence of any anomaly by the pairs S and M, respectively.

The collected data form the 16×16 matrix given by:

$$\mathcal{D}(z)=-\frac{\Delta\sigma|\Delta\Omega|}{\sigma_0^2}\begin{pmatrix} \vec{\jmath}_{S_1}(z)\cdot\vec{\jmath}_{M_1}(z) & \vec{\jmath}_{S_1}(z)\cdot\vec{\jmath}_{M_2}(z) & \dots & \vec{\jmath}_{S_1}(z)\cdot\vec{\jmath}_{M_{16}}(z)\\ \vec{\jmath}_{S_2}(z)\cdot\vec{\jmath}_{M_1}(z) & \vec{\jmath}_{S_2}(z)\cdot\vec{\jmath}_{M_2}(z) & \dots & \vec{\jmath}_{S_2}(z)\cdot\vec{\jmath}_{M_{16}}(z)\\ \vdots & \vdots & \ddots & \vdots\\ \vec{\jmath}_{S_{16}}(z)\cdot\vec{\jmath}_{M_1}(z) & \vec{\jmath}_{S_{16}}(z)\cdot\vec{\jmath}_{M_2}(z) & \dots & \vec{\jmath}_{S_{16}}(z)\cdot\vec{\jmath}_{M_{16}}(z)\end{pmatrix}, \quad (3.74)$$

which can be rewritten as follows:

$$\mathcal{D}(z)=-\frac{\Delta\sigma|\Delta\Omega|}{\sigma_0^2}\begin{pmatrix} j^x_{S_1}(z) & j^y_{S_1}(z)\\ j^x_{S_2}(z) & j^y_{S_2}(z)\\ \vdots & \vdots\\ j^x_{S_{16}}(z) & j^y_{S_{16}}(z)\end{pmatrix}\begin{pmatrix} j^x_{M_1}(z) & j^x_{M_2}(z) & \dots & j^x_{M_{16}}(z)\\ j^y_{M_1}(z) & j^y_{M_2}(z) & \dots & j^y_{M_{16}}(z)\end{pmatrix} \quad (3.75)$$

The vectors $\vec{\jmath}_{S_k}(z)$ and $\vec{\jmath}_{M_k}(z)$ are given by

$$\vec{\jmath}_{S_k}(z)= \frac{I_S}{\pi}\frac{\begin{pmatrix} r\cos\alpha-R\cos\frac{k\pi}{8}\\ r\sin\alpha-R\sin\frac{k\pi}{8}\end{pmatrix}}{\left|\begin{matrix} r\cos\alpha-R\cos\frac{k\pi}{8}\\ r\sin\alpha-R\sin\frac{k\pi}{8}\end{matrix}\right|^2}-\frac{I_S}{\pi}\frac{\begin{pmatrix} r\cos\alpha-R\cos\frac{(k+8)\pi}{8}\\ r\sin\alpha-R\sin\frac{(k+8)\pi}{8}\end{pmatrix}}{\left|\begin{matrix} r\cos\alpha-R\cos\frac{(k+8)\pi}{8}\\ r\sin\alpha-R\sin\frac{(k+8)\pi}{8}\end{matrix}\right|^2}, \quad (3.76)$$

$$\vec{\jmath}_{M_k}(z)= \frac{I_S}{\pi}\frac{\begin{pmatrix} r\cos\alpha-R\cos\frac{k\pi}{8}\\ r\sin\alpha-R\sin\frac{k\pi}{8}\end{pmatrix}}{\left|\begin{matrix} r\cos\alpha-R\cos\frac{k\pi}{8}\\ r\sin\alpha-R\sin\frac{k\pi}{8}\end{matrix}\right|^2}-\frac{I_S}{\pi}\frac{\begin{pmatrix} r\cos\alpha-R\cos\frac{(k+1)\pi}{8}\\ r\sin\alpha-R\sin\frac{(k+1)\pi}{8}\end{pmatrix}}{\left|\begin{matrix} r\cos\alpha-R\cos\frac{(k+1)\pi}{8}\\ r\sin\alpha-R\sin\frac{(k+1)\pi}{8}\end{matrix}\right|^2}, \quad (3.77)$$

where $r=|z|$ and $\alpha=z_1/r$.

In the case of multiple anomalies located at $z_1,\dots,z_m$, the collected data give the matrix $\mathcal{D}(z_1,\dots,z_m)$:

$$\mathcal{D}(z_1,\dots,z_m)=\sum_{j=1}^{m}\mathcal{D}(z_j). \quad (3.78)$$

The singular value decomposition of D writes $D = USV^T$, where

$$U = \begin{pmatrix} \vec{u}^{(1)} & \vec{u}^{(2)} & \dots & \vec{u}^{(16)} \end{pmatrix} = \begin{pmatrix} u_1^{(1)} & u_1^{(2)} & \dots & u_1^{(16)} \\ u_2^{(1)} & u_2^{(2)} & \dots & u_2^{(16)} \\ \vdots & \vdots & \ddots & \vdots \\ u_{16}^{(1)} & u_{16}^{(2)} & \dots & u_{16}^{(16)} \end{pmatrix} \tag{3.79}$$

$$S = diag(s_1, s_2, \dots, s_{16}) = \begin{pmatrix} s_1 & 0 & \dots & 0 \\ 0 & s_2 & \dots & 0 \\ \vdots & \vdots & \ddots & \vdots \\ 0 & 0 & \dots & s_{16} \end{pmatrix} \tag{3.80}$$

$$V = \begin{pmatrix} \vec{v}^{(1)} & \vec{v}^{(2)} & \dots & \vec{v}^{(16)} \end{pmatrix} = \begin{pmatrix} v_1^{(1)} & v_1^{(2)} & \dots & v_1^{(16)} \\ v_2^{(1)} & v_2^{(2)} & \dots & v_2^{(16)} \\ \vdots & \vdots & \ddots & \vdots \\ v_{16}^{(1)} & v_{16}^{(2)} & \dots & v_{16}^{(16)} \end{pmatrix}. \tag{3.81}$$

Further, $V^TV = U^TU = Id_{16}$. The following relation between $\vec{v}^{(k)}$ and $\vec{u}^{(k)}$ holds:

$$\mathcal{D}\vec{v}^{(k)} = USV^T\vec{v}^{(k)} = s_k\vec{u}^{(k)}.$$

Suppose that $s_1 \geqslant s_2 \geqslant \dots \geqslant s_r > s_{r+1} = \dots s_{16} = 0$ and let Range($\mathcal{D}$) denote the space spanned by the vectors $\vec{v}^{(1)}, \dots, \vec{v}^{(r)}$.

3.5.2 Detection of the Centers and the Radius of the Anomalies

We define four vectors $\vec{S}_x(z)$, $\vec{S}_y(z)$, $\vec{M}_x(z)$, and $\vec{M}_y(z)$ as follows:

$$\vec{S}_x(z) = \begin{pmatrix} j^x_{S_1}(z) \\ j^x_{S_2}(z) \\ \vdots \\ j^x_{S_{16}}(z) \end{pmatrix}, \qquad \vec{S}_y(z) = \begin{pmatrix} j^y_{S_1}(z) \\ j^y_{S_2}(z) \\ \vdots \\ j^y_{S_{16}}(z) \end{pmatrix}, \tag{3.82}$$

$$\vec{M}_x(z) = \begin{pmatrix} j^x_{M_1}(z) \\ j^x_{M_2}(z) \\ \vdots \\ j^x_{M_{16}}(z) \end{pmatrix}, \qquad \vec{M}_y(z) = \begin{pmatrix} j^y_{M_1}(z) \\ j^y_{M_2}(z) \\ \vdots \\ j^y_{M_{16}}(z) \end{pmatrix}. \tag{3.83}$$

Set $E_M = \text{span}(\vec{M}_x(z), \vec{M}_y(z))$ and $E_M^\perp$ the vectorial space orthogonal to E_M. Since E_M is of dimension ≥ 2 then $\dim(E_M^\perp) \leq 14$.

Suppose that $\vec{w} \in E_M^{\perp}$. Then, by construction of $\mathcal{D}(z_1, \ldots, z_m)$, we get

$$\mathcal{D}(z_1, \ldots, z_m)\vec{w} = -\frac{\Delta\sigma}{\sigma_0^2} \begin{pmatrix} \vec{S}_x(z_1) & \vec{S}_y(z_1) & \ldots & \vec{S}_x(z_m) & \vec{S}_y(z_m) \end{pmatrix} \cdot$$
$$|\mathbf{\Delta\Omega}| \begin{pmatrix} \vec{M}_x(z_1) & \vec{M}_y(z_1) & \ldots & \vec{M}_x(z_m) & \vec{M}_y(z_m) \end{pmatrix}^T \vec{w} = \vec{0}, \quad (3.84)$$

where $\mathbf{\Delta\Omega}$ is a $2m \times 2m$ diagonal matrix:

$$|\mathbf{\Delta\Omega}| = diag\left(|\Delta\Omega_1|, |\Delta\Omega_1|, \ldots, |\Delta\Omega_m|, |\Delta\Omega_m|\right) \quad (3.85)$$

(3.84) says that $\vec{w} \notin \text{Range}(\mathcal{D})$, which implies that $\dim(\text{Range}(\mathcal{D}))^{\perp} \geq 16 - 2m$. Therefore,

$$Proj\left(\vec{M}_x(z)\middle|\, \mathcal{L}(\vec{v}^{(2m+1)}, \ldots, \vec{v}^{(16)})\right) = \vec{0}, \quad (3.86)$$

$$Proj\left(\vec{M}_y(z)\middle|\, \mathcal{L}(\vec{v}^{(2m+1)}, \ldots, \vec{v}^{(16)})\right) = \vec{0}. \quad (3.87)$$

Set $\mathcal{L} = \mathcal{L}(\vec{v}^{(2m+1)}, \ldots, \vec{v}^{(16)})$. To detect the center of the anomaly, we seek points z that are zeros of the function $g(z)$ given by

$$g(z) = \left|Proj\left(\vec{M}_x(z)\middle|\, \mathcal{L}\right)\right|^2 + \left|Proj\left(\vec{M}_y(z)\middle|\, \mathcal{L}\right)\right|^2. \quad (3.88)$$

Consider now the product $U^T\mathcal{D}V$. From (3.84), it follows that

$$(U^T\mathcal{D}V)_{jj} = \sum_{k=1}^{m} |\Delta\Omega_k|(u^{(j)})^T \left(\vec{S}_x(z_k), \vec{S}_y(z_k)\right) \left(\vec{M}_x(z_k), \vec{M}_y(z_k)\right)^T v^{(j)} = s_j \quad (3.89)$$

which corresponds to the system of linear equations: $\sum_{k=1}^{m} A_{jk}|\Delta\Omega_k| = s_j$, where A_{jk} is given by

$$A_{jk} = (u^{(j)})^T \left(\vec{S}_x(z_k), \vec{S}_y(z_k)\right) \left(\vec{M}_x(z_k), \vec{M}_y(z_k)\right)^T v^{(j)}. \quad (3.90)$$

It is clear that the solution to this system (in the least-square sense) is given by

$$(|\Delta\Omega_1|, \ldots, |\Delta\Omega_m|)^T = (A^TA)^{-1}A^T (s_1, \ldots, s_{16})^T. \quad (3.91)$$

3.5.3 Numerical Tests

For this numerical test, we consider three anomalies placed at $z_j = (r_j, \alpha_j)$, where

$$\begin{cases} z_1 = (r_1, \alpha_1) = (1.105, 20.25^\circ), \\ z_2 = (r_2, \alpha_2) = (2.405, 100.25^\circ), \\ z_3 = (r_3, \alpha_3) = (1.505, 290.25^\circ), \end{cases} \quad (3.92)$$

with radius

$$\begin{cases} d_1 = 0.03, \\ d_2 = 0.04, \\ d_3 = 0.07. \end{cases} \quad (3.93)$$

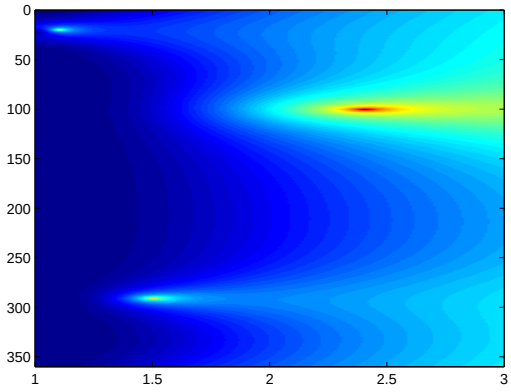

Figure 3.6: Plot of g.

In the Figure 3.6, we plot the values of the function g.

The function g has three peaks at the points:

$$\begin{cases} \widehat{z}_1 = (\widehat{r}_1, \widehat{\alpha}_1) = (1.105, 20.25^\circ), \\ \widehat{z}_2 = (\widehat{r}_2, \widehat{\alpha}_2) = (2.405, 100.25^\circ), \\ \widehat{z}_3 = (\widehat{r}_3, \widehat{\alpha}_3) = (1.505, 290.25^\circ), \end{cases} \tag{3.94}$$

and we can compute the approximate radius:

$$\begin{cases} \widehat{d}_1 = 0.03, \\ \widehat{d}_2 = 0.04, \\ \widehat{d}_3 = 0.07. \end{cases} \tag{3.95}$$

This shows that our algorithm works pretty well.

Now we add noise to test the robustness of our algorithm. We add white Gaussian noise with amplitude γ: we multiply the jk element of the matrix $\mathcal{D}$ by $(1 + \gamma\eta_{jk})$, where the variable η_{jk} is centered gaussian with variance 1.

Figure 3.7 shows the values of g when $\gamma = 0.01$.

We see that two or the three anomalies are still visible. We have lost the one at the largest distance to Ω. The reconstructed locations for the first two ones are given by

$$\begin{cases} \widehat{z}_1 = (\widehat{r}_1, \widehat{\alpha}_1) = (1.115, 20.25^\circ), \\ \widehat{z}_2 = (\widehat{r}_2, \widehat{\alpha}_2) = (1.515, 290.75^\circ), \end{cases} \tag{3.96}$$

and their radius by

$$\begin{cases} \widehat{d}_1 = 0.033, \\ \widehat{d}_2 = 0.070. \end{cases} \tag{3.97}$$

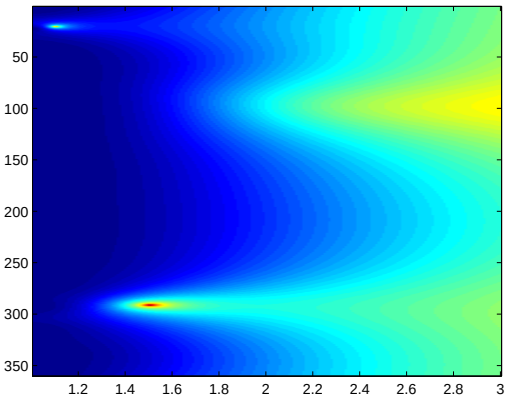

Figure 3.7: Noisy data.

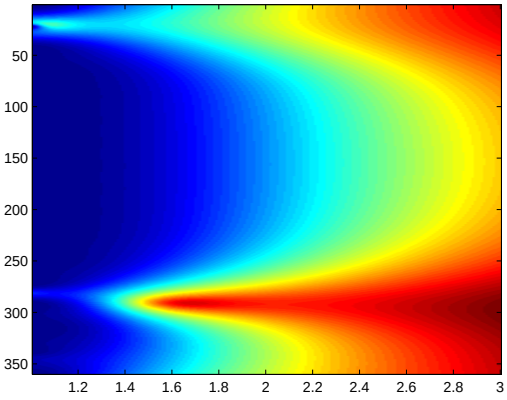

Figure 3.8: Severely noisy data.

In the last test in Figure 3.8, we choose $\gamma = 0.6$.

The detected locations and radius are given by

$$\begin{cases} \widehat{z}_1 = (\widehat{r}_1, \widehat{\alpha}_1) = (1.065, 20.25^\circ), \\ \widehat{z}_2 = (\widehat{r}_2, \widehat{\alpha}_2) = (1.025, 280.75^\circ), \end{cases} \tag{3.98}$$

and

$$\begin{cases} \widehat{d}_1 = 0.020, \\ \widehat{d}_2 = 0.022. \end{cases} \tag{3.99}$$

We see that we can still detect the locations but not any more the radius.

3.6 Concluding Remarks

In this chapter, we have proposed a method to detect anisotropy from higher-order polarization tensors. We have also demonstrated the feasibility of EIET by elastic deformation and presented a method for detecting multiple anomalies from EIET measurements using a realistic electrode model.

Bibliography

[1] W.C. Amalu, W.B. Hobbins, and R.L. Elliot, Infrared imaging of the breast - An overview, Chap. 25 in *Medical Devices and Systems*, The Biomedical Engineering Handbook, 3rd Ed., ed. by J.D. Bronzino, CRC Press, 2006.

[2] H. Ammari, An inverse initial boundary value problem for the wave equation in the presence of imperfections of small volume, SIAM J. Control Optim., 41 (2002), 1194–1211.

[3] H. Ammari, E. Bonnetier, Y. Capdeboscq, M. Tanter, and M. Fink, Electrical impedance tomography by elastic deformation, SIAM J. Appl. Math., to appear.

[4] H. Ammari, Y. Capdeboscq, H. Kang, and A. Kozhemyak, Mathematical models and nreconstruction methods in magneto-acoustic imaging, submitted.

[5] H. Ammari, P. Garapon, H. Kang, and H. Lee, A method of biological tissues elasticity reconstruction using magnetic resonance elastography measurements, Quart. Appl. Math., 66 (2008), 139–175.

[6] H. Ammari, E. Iakovleva, H. Kang, and K. Kim, A direct algorithm for thermal imaging of small inclusions, SIAM J. Multiscale Modeling and Simulation 4 (2005), 1116–1136.

[7] H. Ammari and H. Kang, *Polarization and Moment Tensors: with Applications to Inverse Problems and Effective Medium Theory*, Applied Mathematical Sciences, Vol. 162, Springer-Verlag, New York, 2007.

[8] H. Ammari, H. Kang, and K. Kim, Polarization tensors and effective properties of anisotropic composite materials, J. Diff. Equat., 215 (2005), 401–428.

[9] H. Ammari, A. Kozhemyak, and D. Volkov, Asymptotic formulas for thermography based recovery of anomalies, submitted.

[10] C. Bardos, G. Lebeau, and J. Rauch, Sharp sufficient conditions for the observation, control, and stabilization of waves from the boundary, SIAM J. Control Optim., 30 (1992), 1024–1065.

[11] H. Brezis, Analyse Fonctionnelle: théorie et applications, theorem X.9, Paris; Milan; Barcelone: Masson , 1992.

[12] Y. Capdeboscq, J. Fehrenbach, F. de Gournay, and O. Kavian, An optimal control approach to imaging by modification, preprint.

[13] F.G. Friedlander, *The Wave Equation on a Curved Space-Time*, Cambridge University Press, Cambridge, 1975.

[14] S. Haider, A. Hrbek, and Y. Xu, Magneto-acousto-electrical tomography, preprint.

[15] F. Hetch, O. Pironneau, K. Ohtsuka and A. Le Hyaric, FreeFem++, http://www.freefem.org, 2007.

[16] D. Isaacson, Distinguishability of conductivities by electric current computed tomography, IEEE Trans. Medical Imaging (1986), 91–95.

[17] M.R. Islam and B.C. Towe, Bioelectric current image reconstruction from magneto-acoustic measurements, IEEE Trans. Med. Img. 7 (1988), 386-391.

[18] J. Jossinet, E. Marry, and A. Montalibet, Electrical impedance endo-tomography: imaging tissue from inside, IEEE Trans. Medical Imag., 21 (2002), 560–565.

[19] J. Jossinet, E. Marry, and A. Matias, Electrical impedance endo-tomography, Phys. Med. Biol., 47 (2002), 2189–2202.

[20] H. Kang, E. Kim, and K. Kim, Anisotropic polarization tensors and determination of an anisotropic inclusion, SIAM J. Appl. Math., 65 (2003), 1276-1291.

[21] H. Kang and K. Kim, Anisotropic polarization tensors for ellipses and ellipsoids, J. Comp. Math., 25 (2007), 157–168.

[22] S. Kim, O. Kwon, J.K. Seo, and J.R. Yoon, On a nonlinear partial differential equation arising in magnetic resonance electrical impedance imaging, SIAM J. Math. Anal., 34 (2002), 511–526.

[23] Y.J. Kim, O. Kwon, J.K. Seo, and E.J. Woo, Uniqueness and convergence of conductivity image reconstruction in magnetic resonance electrical impedance tomography, Inverse Problems, 19 (2003), 1213–1225.

[24] A. Kozhemyak, Electrical impedance endo-tomography, submitted.

[25] O. Kwon, J.K. Seo, and J.R. Yoon, A real-time algorithm for the location search of discontinuous conductivities with one measurement, Comm. Pure Appl. Math., 55 (2002), 1–29.

[26] J.C. Lantis II, K.L. Carr, R. Grabowy, R.J. Connolly, and S.D. Schwaitzberg, Microwave applications in clinical medicine, Surg Endosc, 12 (1998), 170–176.

[27] X. Li, Y. Xu, and B. He, Magnetoacoustic tomography with magnetic induction for imaging electrical impedance of biological tissue, J. Appl. Phys., 99 (2006), Art. No. 066112.

[28] X. Li, Y. Xu, and B. He, Imaging electrical impedance from acoustic measurements by means of magnetoacoustic tomography with magnetic induction (MAT-MI), IEEE Transactions on Biomed. Eng., 54 (2007), 323–330.

[29] J.H. Lienhard IV and J.H. Lienhard V, *A Heat Transfer Textbook*, Phlogiston Press, Cambridge, Massachusetts, 2006.

[30] J. L. Lions, Equations différentielles opérationnelles et problèmes aux limites, theorem 1.1, chapter IV and remark 1.2, Berlin, Springer, 1961.

[31] J. L. Lions,Equations différentielles opérationnelles et problèmes aux limites, theorem 3.1 chapter V. And section VI.8, Springer, 1961.

[32] N.R. Miller, J.C. Bamber, and G.R. ter Haar, Ultrasonic temperature imaging for the guidance of thermal ablation therapies: in vitro results, 2002 IEEE Ultrasonic Symposium, 1365–1368.

[33] A. Montalibet, J. Jossinet, A. Matias, and D. Cathignol, Electric current generated by ultrasonically induced Lorentz force in biological media, Medical Biol. Eng. Comput., 39 (2001), 15–20.

[34] Y.R. Parisky, A. Sardi, R. Hamm, K. Hughes, L. Esserman, S. Rust, and K. Callahan, Efficacy of computerized infrared imaging analysis to evaluate mammographically suspicious lesions, American J. Radiology, 180 (2003), 263–269.

[35] B.J. Roth and P.J. Basser, A model of the stimulation of a nerve fiber by electromagnetic induction, IEEE Trans. Biomed. Eng., 37 (1990), 588-597.

[36] B.J. Roth, P.J. Basser, and J.P. Jr Wikswo, A theoretical model for magneto-acoustic imaging of bioelectric currents, IEEE Trans. Biomed. Eng., 41 (1994), 723-728.

[37] A. Sommerfeld, *Partial Differential Equations in Physics*, New York, Academic Press, 1949.

[38] K. Touibi, *Imaging Microstructures*, Ph.D. Thesis, Ecole Polytechnique, 2004.

[39] H. Wen, J. Shah, and Balaban, An imaging method using the interaction between ultrasound and magnetic field, Proc. IEEE Ultrasonics Symp. (1997), 1407–1410.

[40] H. Wen, J. Shah, and Balaban, Hall effect imaging, IEEE Trans. Biomed. Eng., 45 (1998), 119–124.

[41] M. Xua and L.V. Wang, Photoacoustic imaging in biomedicine, Review of Scientific Instruments 77, 041101, 2006.

[42] T. Yahara, T. Koga, S. Yoshida, S. Nakagawa, H. Deguchi, and K. Shirouzu, Relationship between microvessel density and thermographic hot areas in breast cancer, Surg Today, 33 (2003), 243–248.